CHAPTER IV

RESULTS AND DISCUSSION

1. Preparation and Characterizations of Solid Lipid Nanoparticles (SLN)

1.1 SLN Production

The SLN produced according to the generated experiment design possessed diameter in a nanometer range with positive surface charge due to the ionization of an amine group in DDAB molecule as shown in Table 4.1. The appearance of the preparations looked like milky suspension.

Table 4.1 Particle size, PI and zeta potential of SLN (mean±SD)

Formulation	Code of (a, b, c)*	Responses		
		Size (nm)	PI	Zeta potential (mV)
SLN1	(-,-,-)	140±1	0.25±0.01	39±1
SLN2	(+,-,-)	142±3	0.23±0.00	11±0
SLN3	(-,+,-)	160±2	0.37±0.00	58±1
SLN4	(+,+,-)	191±2	0.27±0.00	61±1
SLN5	(-,-,+)	150±2	0.24±0.01	37±1
SLN6	(+,-,+)	147±1	0.32±0.01	16±1
SLN7	(-,+,+)	136±1	0.27±0.00	50±1
SLN8	(+,+,+)	162±2	0.29±0.00	60±2
SLN9	(-α,0,0)	160±2	0.27±0.01	58±1
SLN10	(+α ,0,0)	179±1	0.24±0.01	49±1
SLN11	(0,-α ,0)	142±1	0.32±0.01	22±0
SLN12	(0,+α ,0)	163±1	0.36±0.01	52±1
SLN13	(0,0,-α)	161±1	0.25±0.01	56±1
SLN14	(0,0,+α)	154±2	0.24±0.00	54±1
SLN15	(0,0,0)	166±1	0.24±0.00	50±1
SLN16	(0,0,0)	170±3	0.25±0.00	51±1
SLN17	(0,0,0)	163±2	0.26±0.00	51±1
SLN18	(0,0,0)	169±1	0.26±0.01	51±1

*a, b, c are level of surfactant, DDAB and cholesterol, respectively

In addition, the average particle size, PI and zeta potential shown in Table 4.1 suggested that a fine control of particle size, PI and zeta potential of SLN could be achieved by combination of the three variables; surfactant, DDAB and cholesterol concentration. The scanning electron microscopy (SEM) and transmission electron microscopy (TEM) photograph of SLN15 as a representative of all formulations shown in Figure. 4.1 demonstrated spherical shape of SLN.

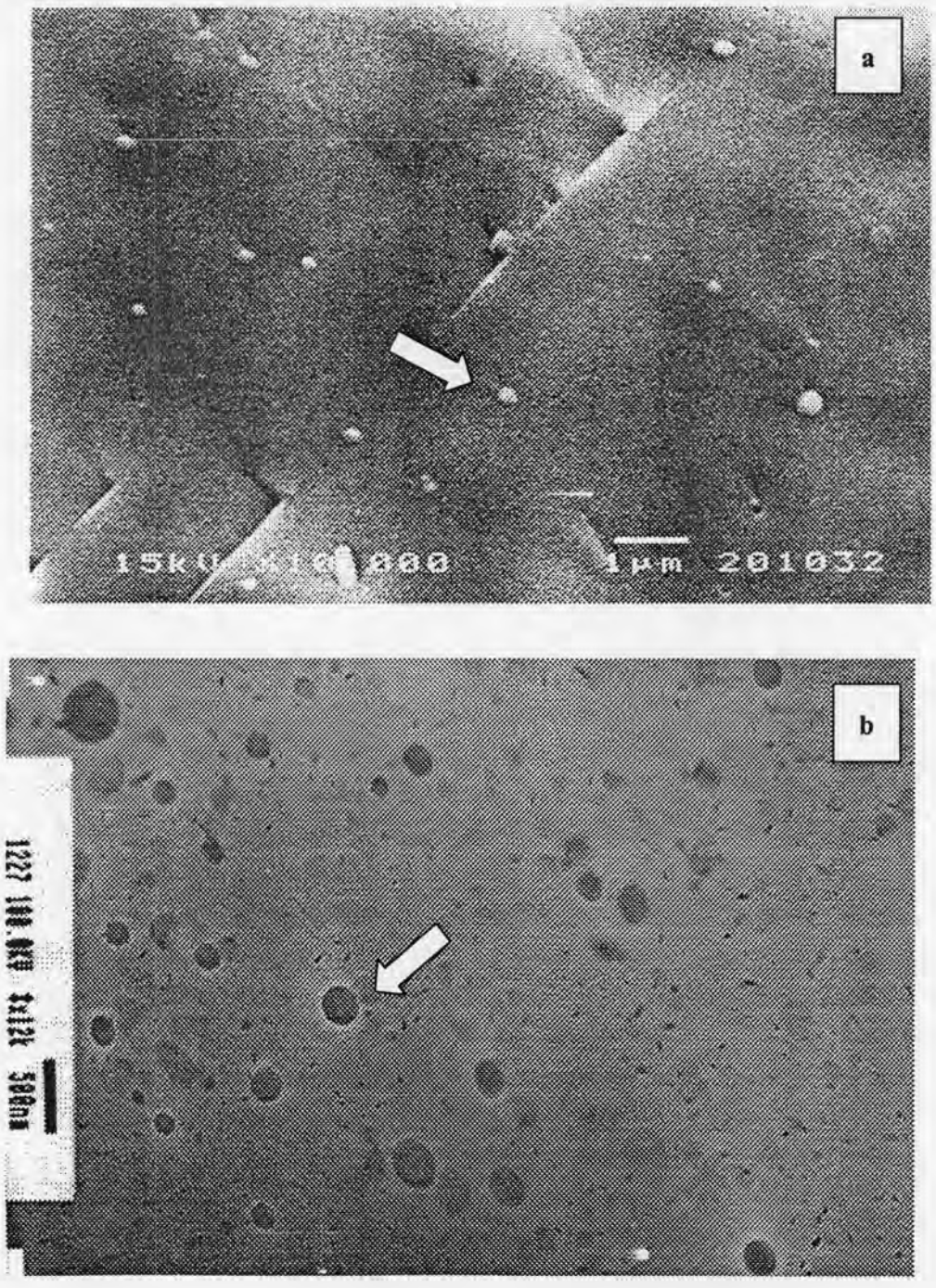

Figure 4.1 Photograph of SLN 15: (a) SEM (x10,000) and (b) TEM (x12,000).

1.2 The Experimental Design

The regression analysis of the results generated the following polynomial equations which the model *F* ratios were statistically significant at $p<0.05$ with Adj-R^2 value in the range of 0.8-1 and were non statistically significant lack of fit at $p>0.05$.

$$\text{Particle size} = 144.36-6.17a+58.03b+51.28c+0.60a^2-37.23b^2-53.64c^2+4.18ab-44.22bc \quad (4.1)$$

$$PI = 0.24+0.02a-0.15b+0.10c-0.002a^2+0.21b^2-0.23c^2-0.01ab+0.02ac-0.11bc \quad (4.2)$$

$$\text{Zeta potential} = 46.93-7.07a+67.40b-25.85c+0.20a^2-46.93b^2+27.88c^2 +4.64ab+1.90ac-7.79bc \quad (4.3)$$

Where a, b, c are concentrations of surfactant, DDAB and cholesterol, respectively.

Table 4.2 Statistical analysis of the experimental design

Responses	Sources		
	Model *p* value	Adj-R^2	Lack of fit test *p* value
Particle size	<0.0001	0.9502	0.5470
PI	0.0003	0.8866	0.1010
Zeta potential	<0.0001	0.9982	0.4125

The statistical analysis results shown in Table 4.2 suggested that there was less than 0.01% chance that the model *F* value of model equation (4.1) and (4.3) occurred due to noise while 0.03% chance for the model equation (4.2). Their Adj-R^2 showed that the model equation (4.1), (4.2) and (4.3) could explain 95.02%, 88.66% and 99.82%, respectively, of the variability. The *p* values of the lack of fit test of the three models were not significant. This pointed out that these model equations fitted the data well. However, the fit of these model equations for the responses were confirmed by the following diagnostic plots: 1) normal %probability plot of the studentized residuals, 2) studentized residuals versus predicted values, 3) outliers plots and 4) plot of residuals in time sequence, generated by the Design-Expert V. 6 software.

1) Normal %probability plot of the studentized residuals

DESIGN-EXPERT Plot

(a): size

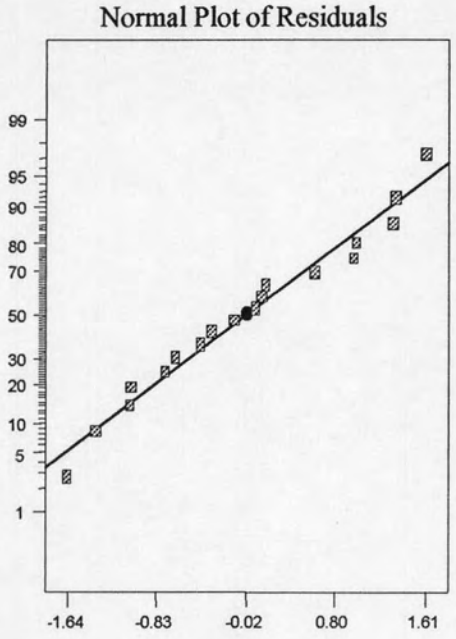

X: Studentized Residuals
Y: Normal % Probability

DESIGN-EXPERT Plot

(b): PI

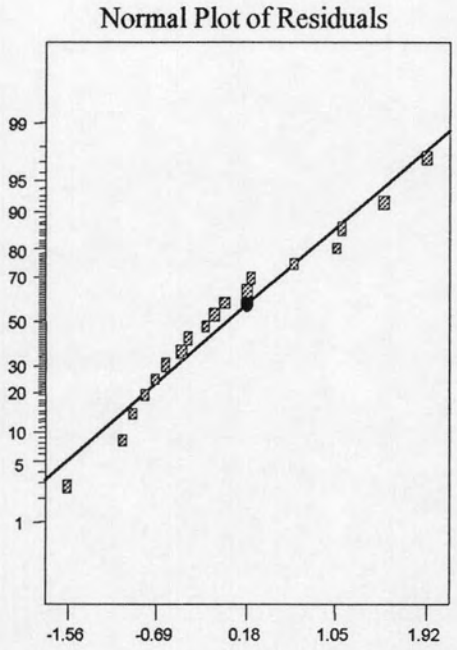

X: Studentized Residuals
Y: Normal % Probability

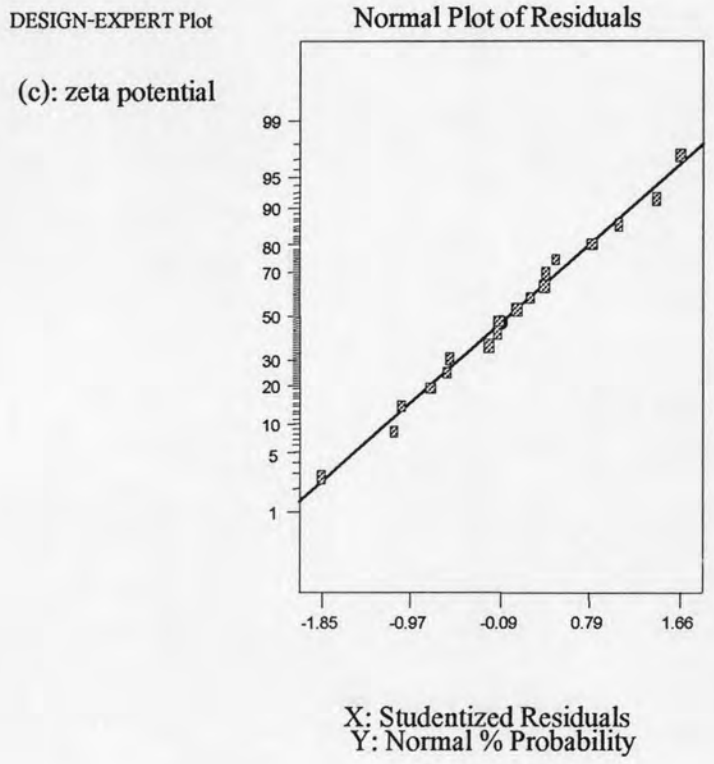

Figure 4.2 Normal % probability plot of the model equations for (a) size, (b) PI and (c) zeta potential.

An analysis of the residuals for checking the normality assumption was performed by plotting the normal %probability versus studentized residual as shown in Figure 4.2. It was found that the normal %probability plot of all model equations were straight line. This implied that the residuals were normally distributed (Rambali, Baert and Massart, 2001). Moreover, there were no any residuals that were abnormally larger than any of the others presented in the plots. This suggested that there was no an outlier which might influence on the model properties.

Montgomery (2005) suggested that the presence of one or more outliers can seriously distort the analysis of variance, so when a potential outlier is located, careful investigation is called for. Frequently, the cause of the outlier is a mistake in calculations or a data coding or copying error. If this is not the cause, the experimental circumstances surrounding this run must be carefully studied. If the outlying response is a particularly desirable value, the outlier may be more informative than the rest of the data.

2) Studentized residuals versus predicted values

DESIGN-EXPERT Plot

(a): size

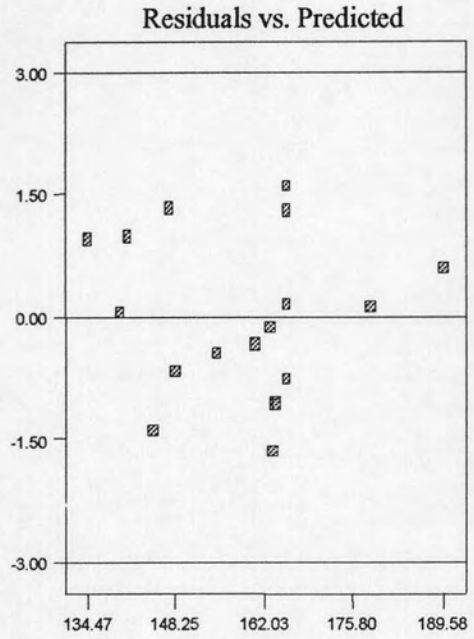

X: Predicted
Y: Studentized Residuals

DESIGN-EXPERT Plot

(b): PI

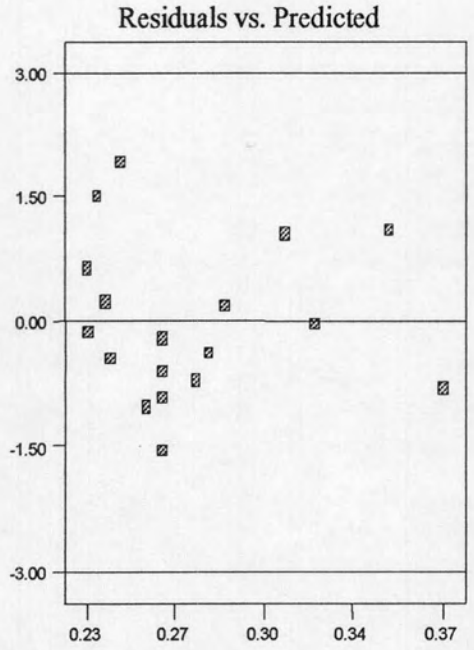

X: Predicted
Y: Studentized Residuals

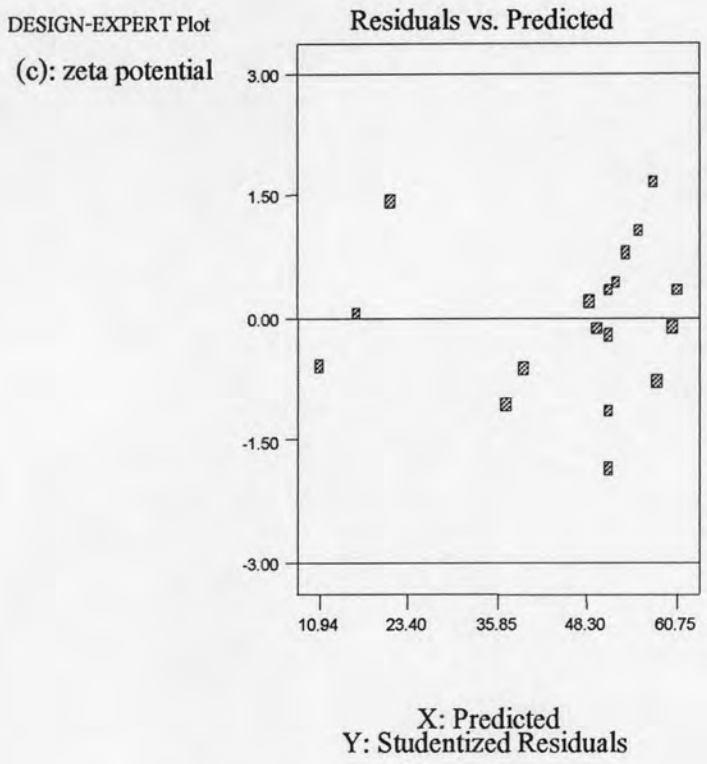

Figure 4.3 Plots of studentized residuals versus predicted values of the model equations for (a) size, (b) PI and (c) zeta potential.

The plots of studentized residuals versus predicted values shown in Figure 4.3 are structureless. That means the model equations were correct and also the normality assumption was satisfied. Montgomery (2005) also suggested that if the model is correct and if the normality assumption is satisfied, the plots of studentized residuals versus predicted values should not reveal any obvious pattern which might occur when a defect shows up because of the non constant variance.

Sometimes, the variance of the observations increases as the magnitude of the observation increases. This would be the case if the error or background noise in the experiment was a constant percentage of the size of the observation. If this were the case, the residuals would get larger as the observation data gets larger, and the plot of residual versus predicted data looks like an outward-opening funnel or megaphone. Non constant variance also arises in case where the data follow a non-normal skewed distribution because in skewed distribution the variance tends to be function of the mean.

3) Outliers determination

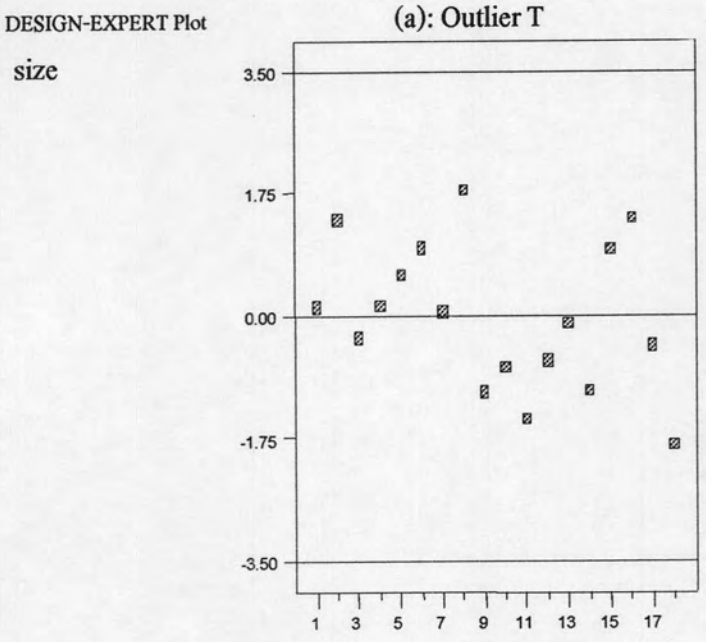

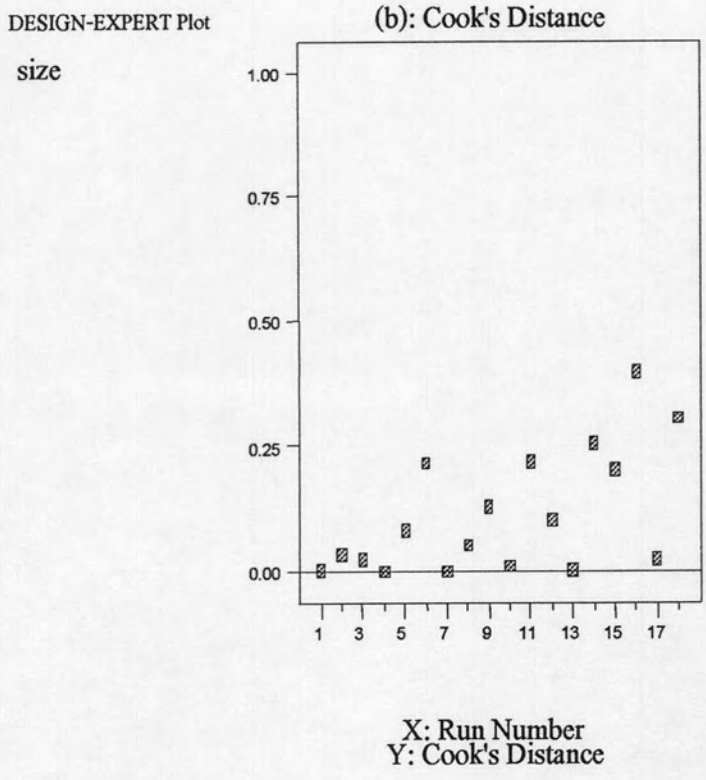

Figure 4.4 (a) Outlier T plot and (b) Cook's distance plot for size's model equation.

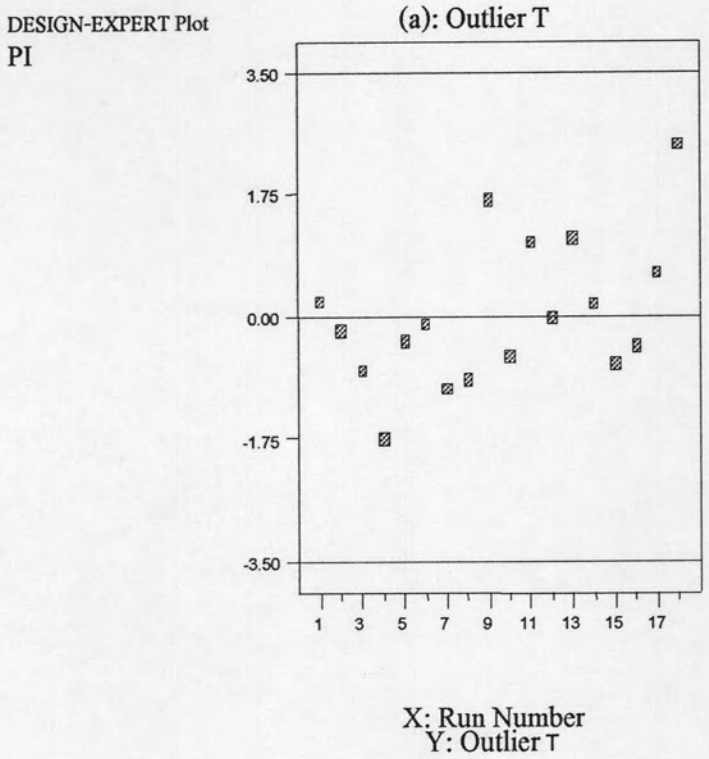

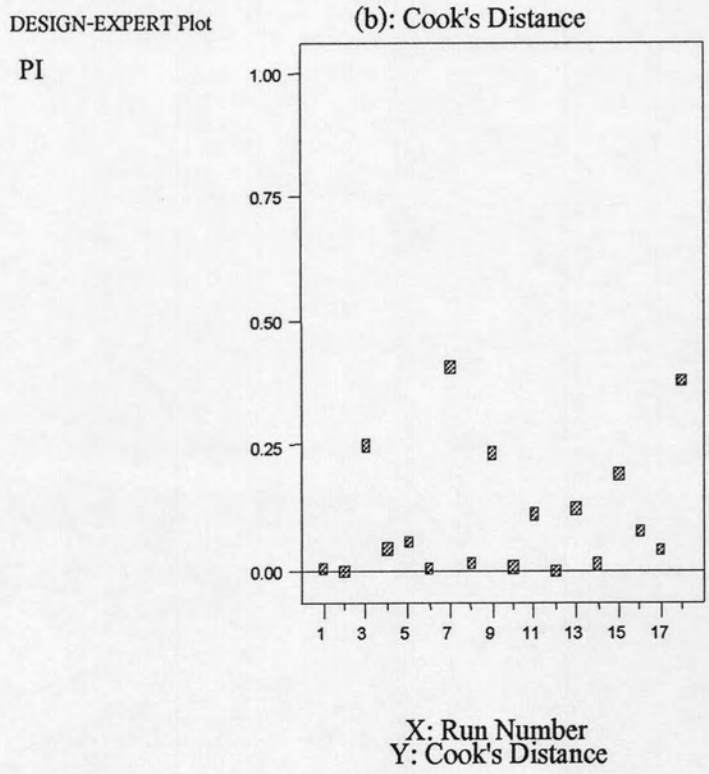

Figure 4.5 (a) Outlier T plot and (b) Cook's distance plot for PI's model equation.

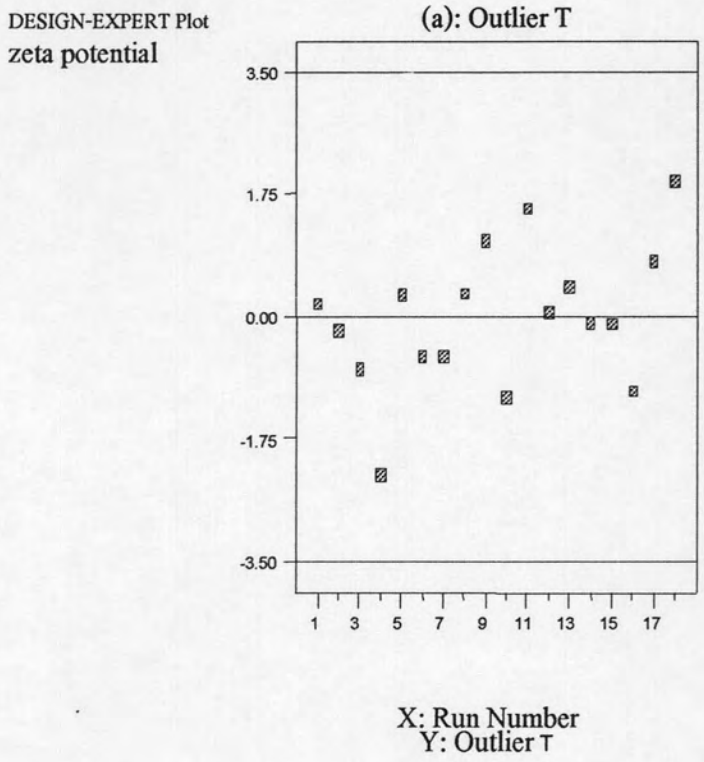

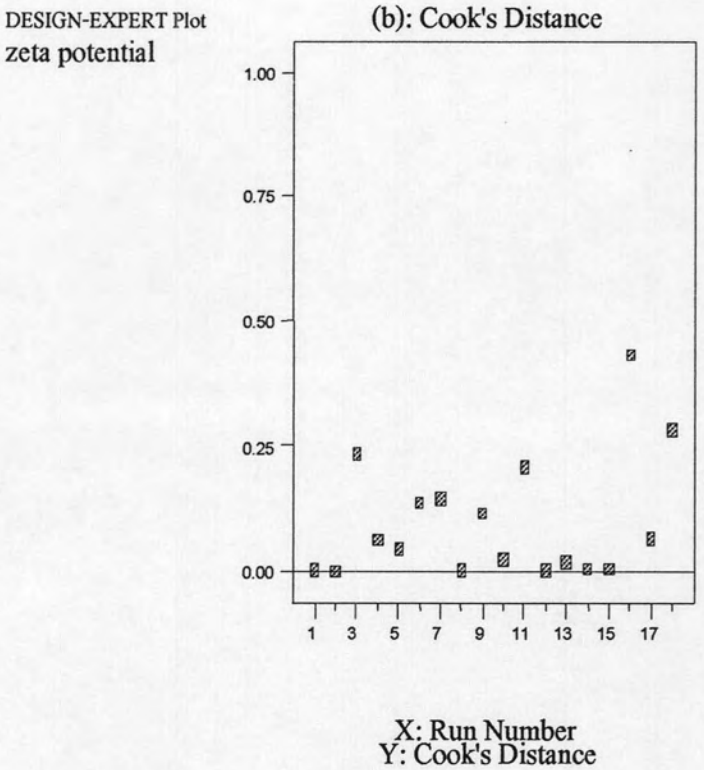

Figure 4.6 (a) Outlier T plot and (b) Cook's distance plot for zeta potential's model equation.

The outlier T plot for the model equations in Figure 4.4 (a)-4.6 (a) show that all of residuals fell within ±3. That means there was no a potential outlier occurring in all of generated models. Generally, a residual bigger than ±3 or ±4 from zero is accepted as a potential outlier (Montgomery, 2005). The Cook's distance plot in Figure 4.4 (b)-4.6 (b) show the consistent results with the outlier T plots. It was found that the Cook's distances of all residuals were less than 1 implying no abnormal influence data occurring.

4) Plot of residuals in time sequence

Figure 4.7 displays the residuals and the time sequence of data collection for size, PI and zeta potential data. It is helpful in detecting correlation between the residuals.

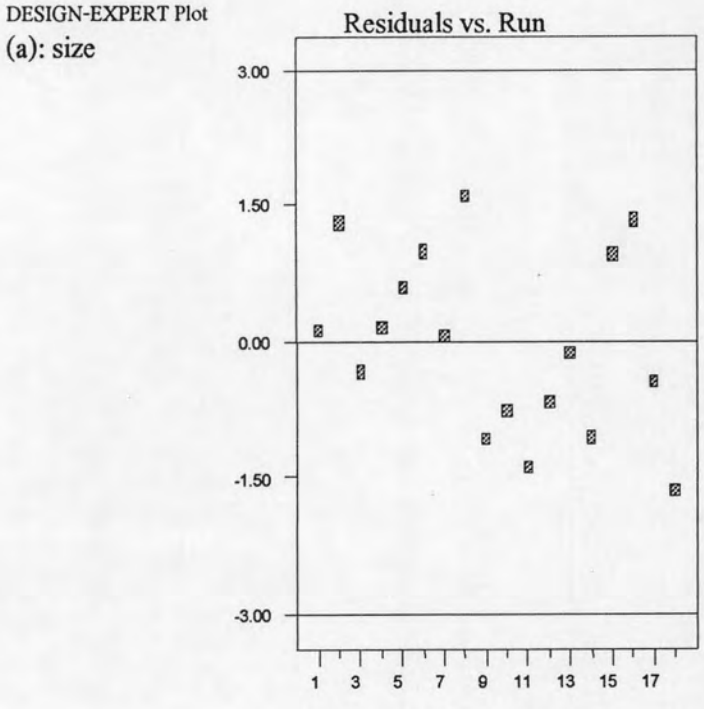

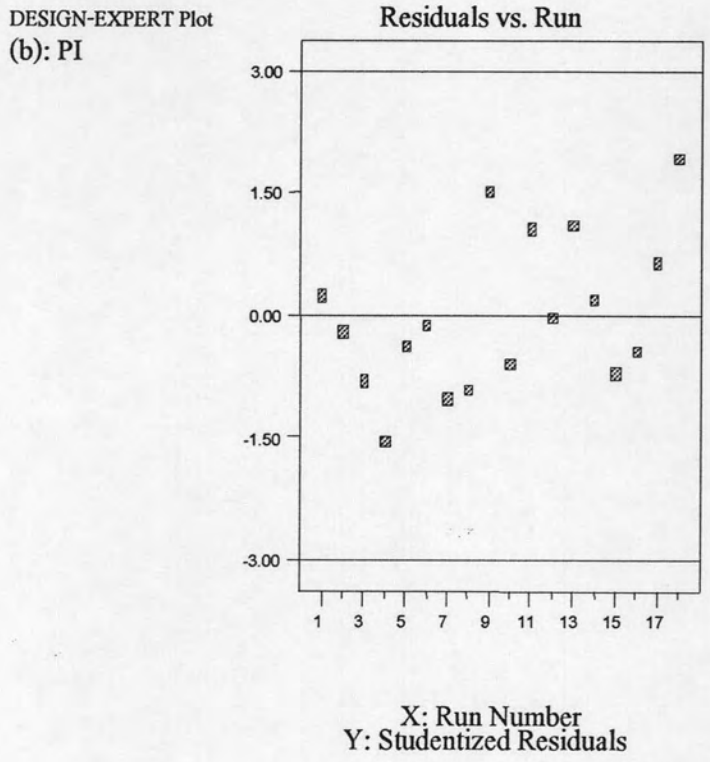

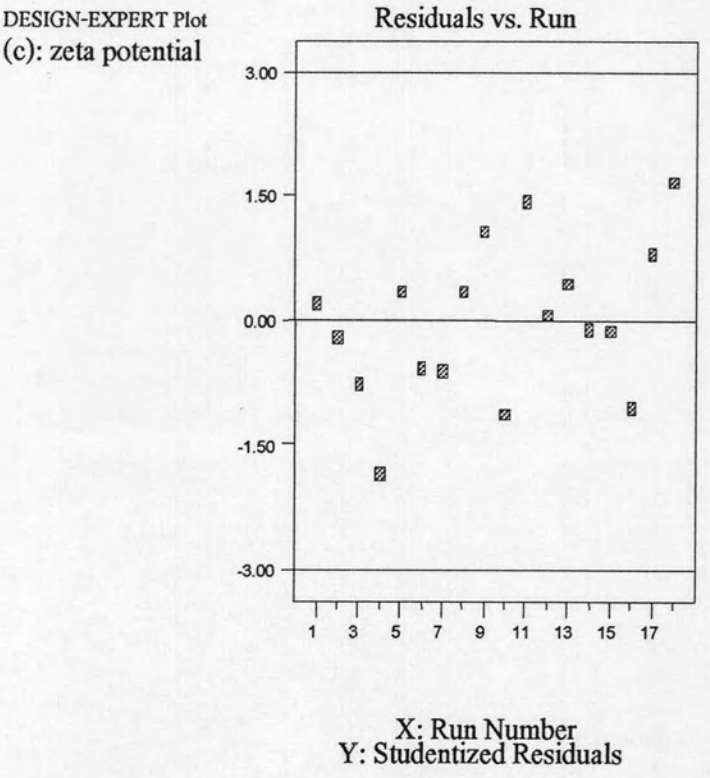

Figure 4.7 Plots of residuals in time sequence of the model equations for (a) size, (b) PI and (c) zeta potential.

The plots of residuals versus time shown in Figure 4.7 do not indicate any tendency. This suggested that there is no reason to suspect any violation of the independence or constant variance assumptions. Because a tendency to have runs of positive and negative residuals indicates a correlation, the independence assumption on the errors has been violated. This leads to a potentially serious problem and one that is difficult to correct.

Therefore, the three quadratic models could describe adequately the data and could be used to navigate the design space.

The model verifications were performed by selecting the required points of factors providing the required points of responses and calculated by the software (optimization-point prediction mode). The results are shown in Table 4.3 and compared to observed value suggesting that these model equations could be used to predict the required optimum size, PI and zeta potential of SLN.

Table 4.3 Comparison of observed values and predicted values of responses (mean±SD, n=3)

Factors (a, b, c)*	Observed value			Predicted value			*p*- value
	Size (nm)	PI	Zeta potential (mV)	Size (nm)	PI	Zeta potential (mV)	
(5, 0.24, 0.34)	156±2	0.30±0.01	33±1	153	0.28	33	<0.05
(5, 0.08, 0.34)	140±2	0.30±0.01	22±1	145	0.31	21	<0.05
(5, 0.16, 0.00)	145±2	0.28±0.01	29±1	140	0.25	30	<0.05
(5, 0.16, 0.68)	151±2	0.31±0.01	31±1	145	0.28	31	<0.05

*a, b, c are concentration of surfactant, DDAB and cholesterol, respectively

However, the model equations containing significant interaction terms of the three variables suggested that the main effect of each variable on particle size, PI and zeta potential of SLN was interfered with the effect of another variable. The three-dimensional response surfaces and contours were plotted on the basis of the model equations to depict the effect of model variables i. e. surfactant, DDAB and cholesterol concentration on particle size, PI and zeta potential.

1.3 Effect of Formulation Compositions on Particle Size, PI and Zeta potential of SLN

1.3.1 Effect of Surfactant and DDAB on Particle Size, PI and Zeta potential of SLN

At the high level of DDAB (Figure 4.8), the increment of surfactant content markedly increased the particle size of SLN. This was probably that DDAB, an amphiphilic compound, could be adsorbed and located more at the interface between oil droplet and water phase as the surfactant content increased. This phenomenon also led to higher zeta potential of SLN as shown in the effect of surfactant and DDAB on zeta potential of SLN (Figure 4.10). Therefore, the obtained nanoparticles would be larger and possessed more positive surface charge. Moreover, the excess surfactant accumulating at the SLN surface also increased the particle size of SLN similarly to a previous study indicating the effect of phospholipids content on size and zeta potential of glyceryl tripalmitate SLN (Schubert and Müller-Goymann, 2005).

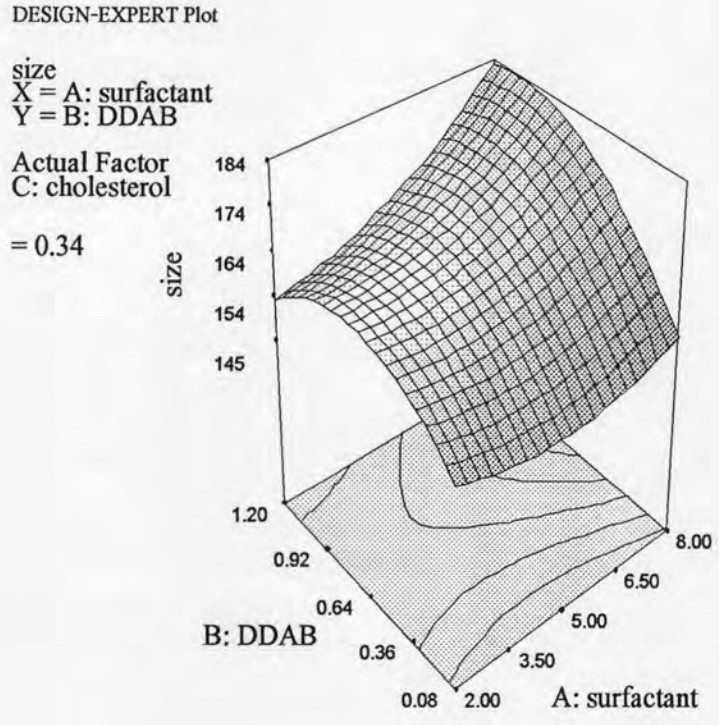

Figure 4.8 Response surface for size of SLN: the effect of surfactant and DDAB.

At the lower level of DDAB, the size of SLN slightly decreased with the increase in surfactant content to about 5%. This might be a consequence of lower interfacial tension between oil phase and water phase by surface active agents resulted in increment of surface curvature of

smaller oil droplets (Goloub and Pugh, 2005). However, at surfactant content above 5%, the size of SLN was increased which could be attributed to the accumulation of excess surfactant molecules at nanoparticle surface.

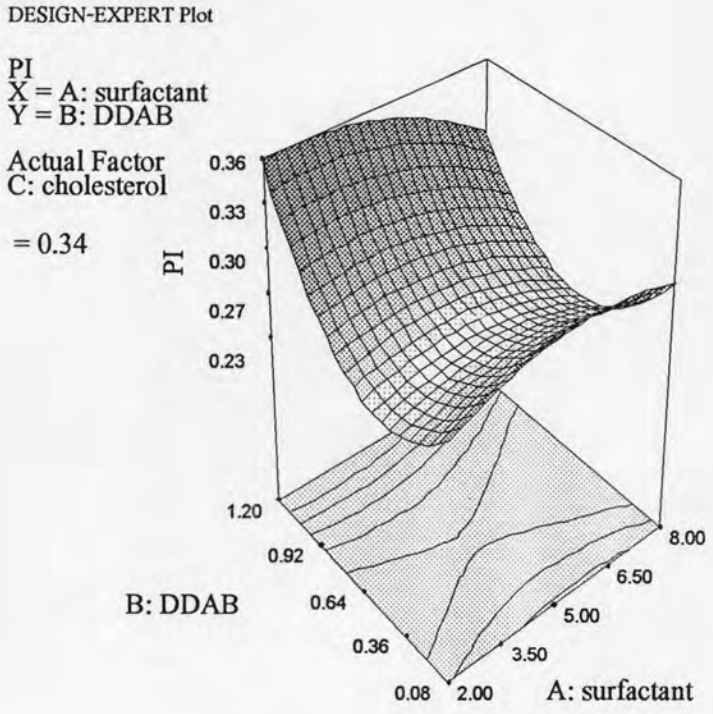

Figure 4.9 Response surface for PI of SLN: the effect of surfactant and DDAB.

Figure 4.9 shows that the increment of surfactant content in SLN consisting of high level of DDAB caused the PI of obtained SLN gradually decreased. This might be that the cationic lipid, DDAB, at high content could act as a surfactant synergizing the effect of surfactant to produce homogeneous oil droplets leading to homogenous SLN after cooling down. On the other hand, PI of SLN with low DDAB content increased with the increment of surfactant until the surfactant content reached 6.5%, it tended to decline. It was possible that at low level of DDAB, only the surfactant could reduce the surface tension of the system. In addition, the increment of surfactant led to the heterogeneous deposition of surfactant around surface of SLN until surfactant content was greater than 6.5%, deposition of surfactant might be more homogeneous. However, it was found that the SLN containing high content of DDAB tended to possess more PI value than

those of the SLN with low content of DDAB. This might due to the excess DDAB deposited on SLN surface more heterogeneously.

The effect of surfactant and DDAB on zeta potential of SLN (Figure 4.10) shows that an increment of surfactant content at the high level of DDAB gradually increased the zeta potential of SLN from 50 mV to 58 mV.

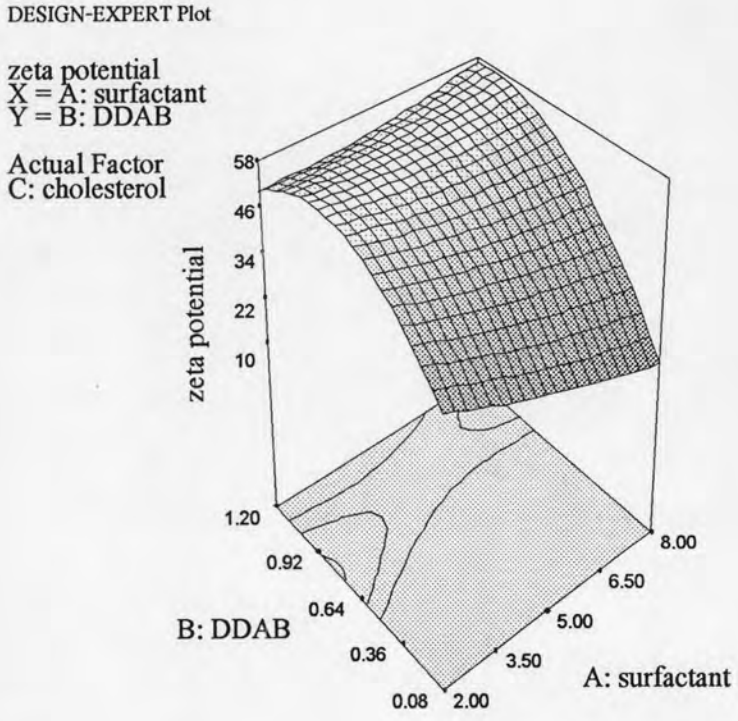

Figure 4.10 Response surface for zeta potential of SLN: the effect of surfactant and DDAB.

This was probably due to DDAB molecules could be adsorbed and located more at the interface of oil droplet as surfactant content increased. At the lower level of DDAB, the increased surfactant content markedly reduced the positive surface charge due to the head group of DDAB at interface might be shielded by the head group of surfactant adsorbed at interface and also the surfactant molecules accumulating around the SLN surface.

1.3.2 Effect of Surfactant and Cholesterol on Particle Size, PI and Zeta potential of SLN

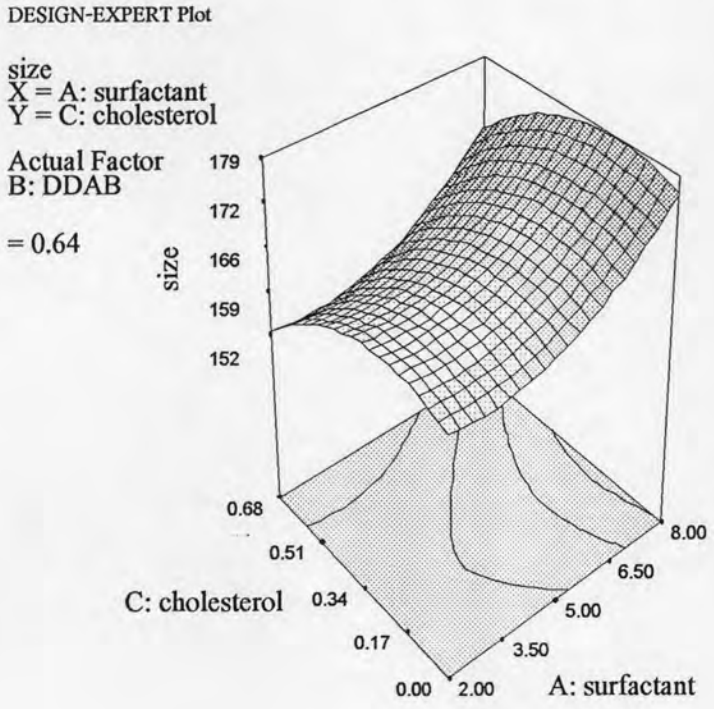

Figure 4.11 Response surface for size of SLN: the effect of surfactant and cholesterol.

As seen in Figure 4.11, the size of SLN with and without cholesterol increased in the same manner with the increment of surfactant content. This showed that cholesterol did not affect the main effect of surfactant on the size of SLN. However, it was found that the SLN containing high level of cholesterol tended to possess smaller particle size than those of the SLN without cholesterol. This result was in accordance with previous study by Jain et al. (2005) showing that the high ratio of cholesterol/lipid matrix reduced the SLN diameter. It might be that the cholesterol incorporated in SLN interacted with surface active molecules at the interface of oil droplets. This led to a rigid surfactant layer including decrement in van der Waal attraction and promotion of net repulsion forces between oil droplets, therefore, agglomeration and coalescence of small oil droplets were reduced. This phenomenon was also found in liposome system consisting of phospholipids and cholesterol (De Souza and Teschke, 2003). In addition, the interaction between cholesterol and surfactant might increase in surface curvature of oil droplet and leading to small size of SLN after cooling down.

At high level of cholesterol (Figure 4.12), the increment of surfactant caused increasing in PI of SLN. This might be that the cholesterol incorporated in SLN could be embed in either lipid core or surfactant layer surrounding SLN surface leading to less uniformed SLN. The PI of SLN without cholesterol (low level) tended to decrease with an increase in surfactant content. This showed that surfactant in the SLN system containing medium content of DDAB (0.64%) without cholesterol addition could promote the homogeneity of SLN particle.

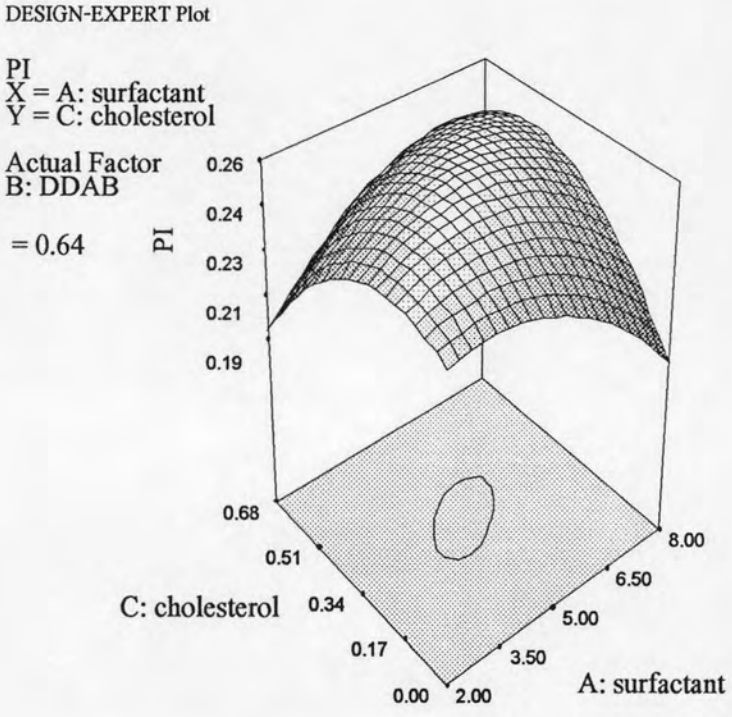

Figure 4.12 Response surface for PI of SLN: the effect of surfactant and cholesterol.

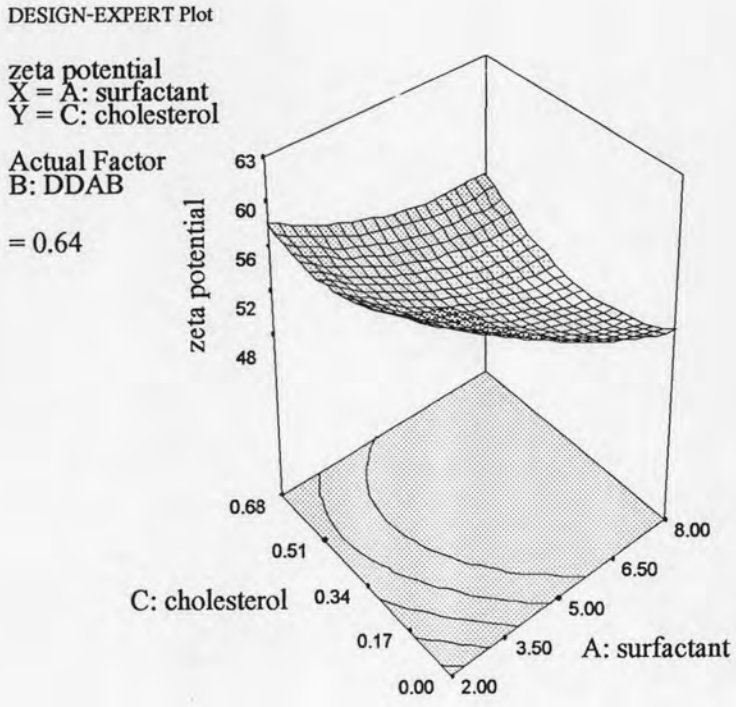

Figure 4.13 Response surface for zeta potential of SLN: the effect of surfactant and cholesterol.

It can be seen in Figure 4.13 that by increasing the surfactant content, the zeta potential of all nanoparticles was reduced. This could be explained by the adsorption and the accumulation of surfactant molecules on the surface of nanoparticle. At the surfactant concentration of less than 6.5%, SLN without cholesterol had more positive surface charge than SLN containing cholesterol. It was possible that the presence of cholesterol in lipid matrix might limit DDAB lipophilic chain partitioning into lipid core, thus the number of DDAB molecules adsorbed at interface were reduced. Nevertheless, at the concentration of surfactant higher than 6.5%, SLN with cholesterol possessed higher zeta potential. This might be due to the effect of cholesterol on the arrangement of surfactant molecules and DDAB molecules at the interface of oil droplet. Therefore, the head group of DDAB was less shielded by the head group of surfactant and surfactant molecules.

1.3.3 Effect of DDAB and Cholesterol on Particle Size, PI and Zeta potential of SLN

The size of SLN containing high level of cholesterol increased with the increment of DDAB content to 0.64% as shown in Figure 4.14.

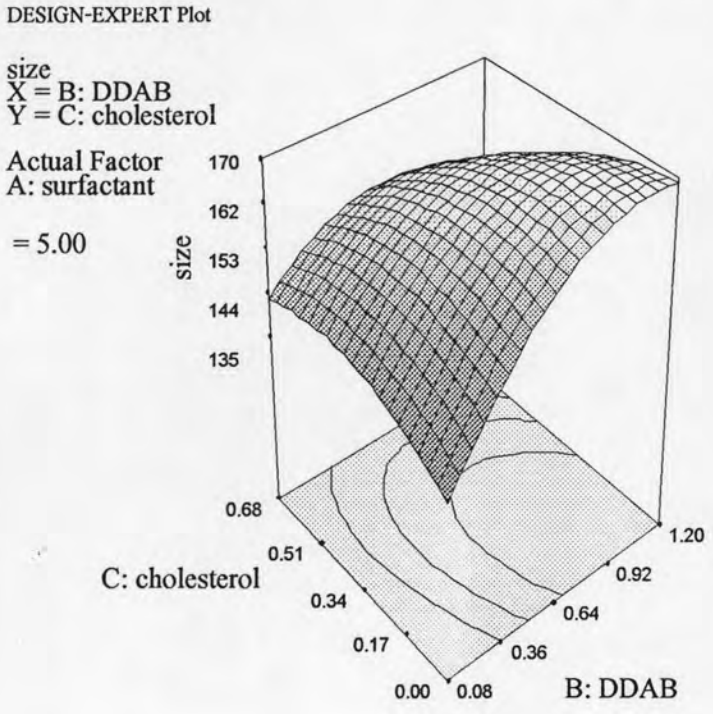

Figure 4.14 Response surface for size of SLN: the effect of DDAB and cholesterol.

This was possible that more DDAB molecules adsorbed at the interface between oil phase and water phase, thus resulting in particle size increment. However, the increase in DDAB content more than 0.64% led to a reduction of particle size of SLN closed to the system containing low content of DDAB. As previously discussed, it might be that cholesterol markedly affected the arrangement of the increased DDAB molecules at the interface of oil droplets resulting in smaller SLN. This result was confirmed by the continuous increment of particle size of SLN without cholesterol as DDAB content increased.

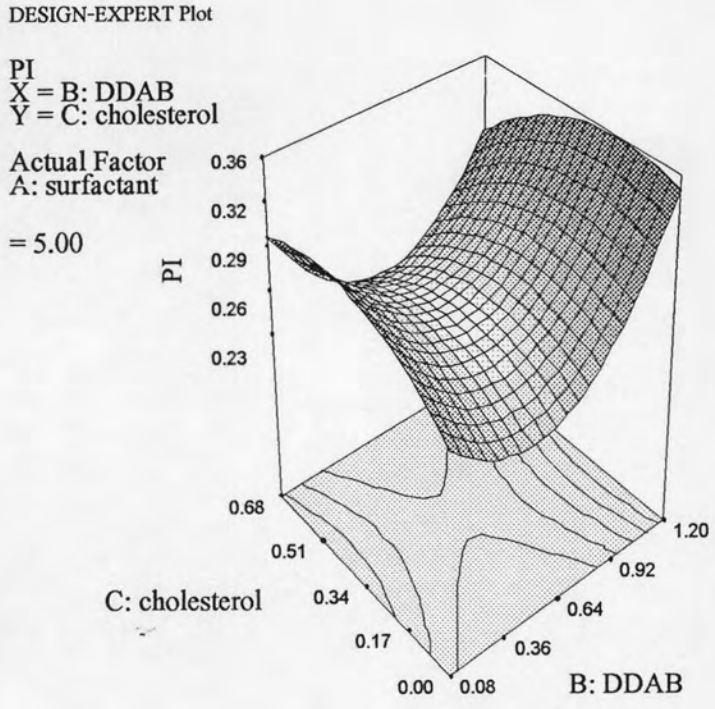

Figure 4.15 Response surface for PI of SLN: the effect of DDAB and cholesterol.

It was found that the homogeneity of SLN with and without cholesterol increased with increment of DDAB to 0.36% as seen in Figure 4.15 and decreased with continuous increment of DDAB. This confirmed that the optimum content of DDAB would promote uniformity of SLN.

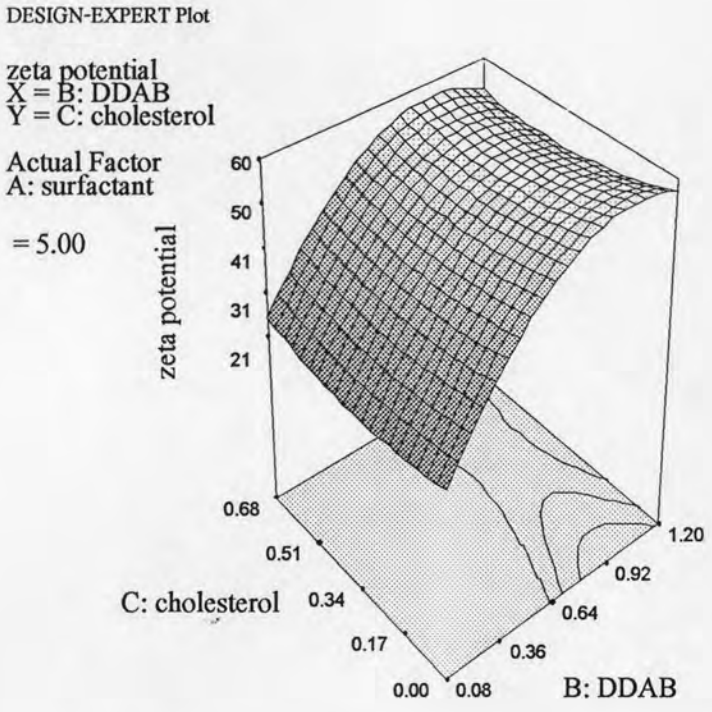

Figure 4.16 Response surface for zeta potential of SLN: the effect of DDAB and cholesterol.

The Figure 4.16 suggests that the increment of DDAB concentration markedly increased the zeta potential of both with and without cholesterol SLN systems. This was a result of the rise in charge density of adsorption layer upon the increase in DDAB molecules at interface which was consistent with the effect of dodecyl pyridinium chloride on zeta potential of oil-in-water emulsion system studied by Goluob and Pugh (2005). Further increase of DDAB concentration gradually increased the zeta potential to reach its maximum value at DDAB concentration of 0.92% and finally, it tended to be stable. This suggested that the saturation of cationic lipid adsorption occurred when the zeta potential reached a maximum and the surface of SLN was completely covered with DDAB molecules. Gu, and Li (1998), Ahlin, Kristl, and Smid-Korbar (1998) also demonstrated a similar saturation plot pattern for zeta potential of silicone-oil-in-water emulsion droplets versus concentration of cetyltrimethylammonuim bromide (CTAB) and glyceryl tripalmitate SLN versus phospholipid content, respectively.

1.4 Differential Scanning Calorimetry (DSC) and X-ray Diffraction (XRD) Analysis of SLN

Although the particle size, PI and zeta potential analysis are the necessary, they are not the sufficient step to characterize SLN quality. Mehnert and Mäder (2001) suggested that a special attention should be paid to the investigation of crystalline state of lipid matrix because this parameter is strongly correlated with drug incorporation and release rate. In addition, based on the assumption that the solidification of the molten lipid particles homogenized has been completed at room temperature, this is the way for proving that the lipid matrix was in solid state at room temperature which is an important character of the true SLN prepared by melt-homogenization (Westesen and Bunjes, 1995). Therefore, the objective of DSC and XRD analysis of SLN in this study was to check the state of lipid matrix at room temperature.

Figure 4.17 shows an overview of the melting process of cetylpalmitate, DDAB, cholesterol and SLN15. For the bulk cetylpalmitate, DDAB and cholesterol, the melting process took place with maximum peak at 54.78 °C, 84.07 °C and 147.91°C, respectively, and at 53.86 °C for SLN15.

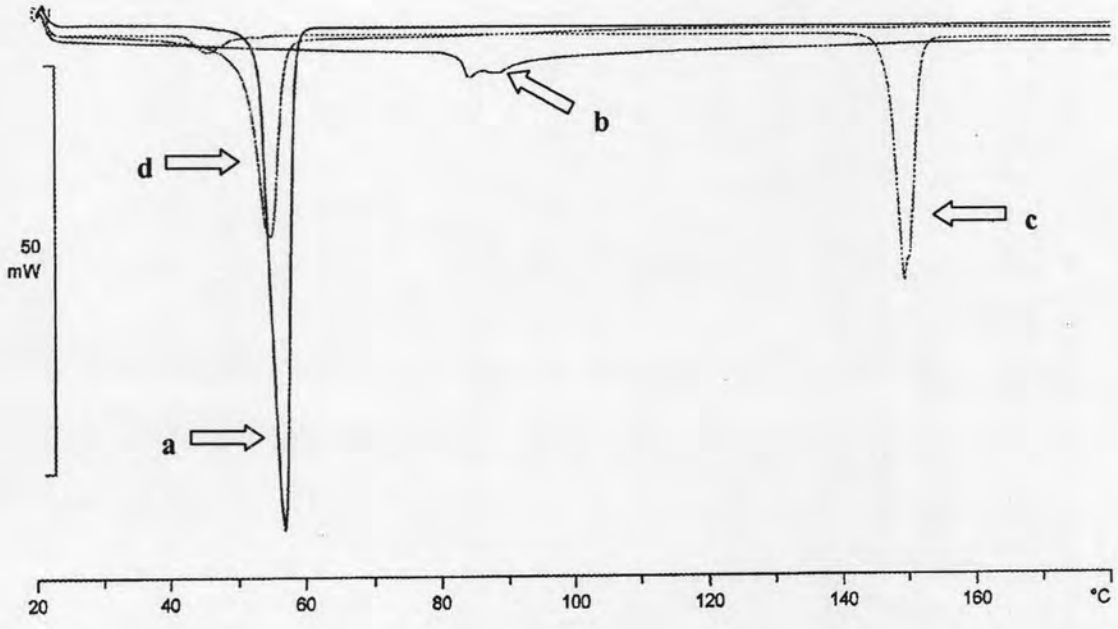

Figure 4.17 Superimposition of DSC thermograms of (a) cetylpalmitate, (b) DDAB, (c) cholesterol and (d) SLN15.

It was observed that only melting peak of cetylpalmitate was found in SLN15 thermogram. This suggests that cholesterol and DDAB dispersing in SLN was in an amorphous form while cetylpalmitate was in a crystalline form. However, the area under peak of cetylpalmitate in SLN15 DSC thermogram was smaller than the area under peak of cetylpalmitate in bulk material DSC thermogram and the peak also shifted to a lower temperature. That means the crystalline form of cetylpalmitate in SLN was less ordered than the bulk cetylpalmitate. Similar findings were found from the melting enthalpy of SLN samples compared to bulk cetylpalmitate shown in Table 4.4.

Table 4.4 Thermal analysis data of bulk materials and SLN (mean±SD, n=3)

Bulk materials/formulation	Melting temperature (°C)	Melting enthalpy (J/g)
Cetylpalmitate	54.78±0.09	242.11±0.10
DDAB	84.07±0.16	15.40±0.46
Cholesterol	147.91±0.07	73.35±0.08
SLN9	53.69±0.06	132.90±0.92
SLN10	50.31±0.03	55.44±0.11
SLN11	51.15±0.05	73.73±0.03
SLN12	53.22±0.05	74.49±0.06
SLN13	54.29±0.12	89.35±0.11
SLN14	53.84±0.05	105.29±0.04
SLN15	53.86±0.02	80.29±0.04

As described in the materials and methods chapter, the SLN9, SLN10, SLN11, SLN12, SLN13, SLN14 and SLN15 were selected as representatives of all formulations because they contained extreme content of interesting factor with medium level of another factors.

All of SLN formulations possessed lower melting point and melting enthalpy compared to bulk cetylpalmitate. This shows that the cetylpalmitate in SLN required less energy than the cetylpalmitate in bulk material to overcome lattice force indicating that the crystals of cetylpalmitate in SLN were less ordered than that of bulk cetylpalmitate (Hou et al., 2003). The decline of melting temperature and melting enthalpy of cetylpalmitate in SLN can be explained by the small particle size effect. Due to small size of SLN in the nanometer range led to their

high specific surface area, cetylpalmitate molecules close to the surface are in a higher energetic state than in the bulk. As a result, small crystals melt at a lower temperature (Siekmann and Westesen, 1994). In addition, the presence of many ingredients in SLN system can also alter the order of cetylpalmitate crystals in SLN leading to the retardation of crystallization after cooling down to room temperature (Mehnert and Mäder, 2001). A previous study showed that the polymorphic transitions of some kinds of lipid matrix such as trimyristin, trilaurin occurred very slowly and remained as a supercool melt over several months at room temperature after they had been molten and homogenized. Therefore, the nanoparticle dispersions from these lipid matrixes were not obtained as dispersions of solid particles but as emulsions of supercool melts and actually, they were not valid for solid lipid nanoparticles (Westesen and Bunjes., 1995). The data shown in Table 4.4 suggested that all of SLN formulations studied by DSC technique were in solid state at room temperature because their melting point was over the room temperature. Therefore, they could be accepted as the true SLN at room temperature. However, apart from the DSC analysis, the state of lipid matrix of SLN was confirmed by XRD technique. The SLN containing high surfactant content (SLN10), high DDAB content (SLN12) and high cholesterol content (SLN14) were selected as the representatives. Their XRD patterns compared to bulk cetylpalmitate were shown in Figure 4.18.

The XRD pattern of bulk cetylpalmitate depicted in Figure 4.18 shows the typical nature of cetylpalmitate crystal. It exhibits sharp peaks at 2θ scattered angles of 6.04, 6.80, 10.12, 11.40, 15.92, 21.65, 23.84, 39.32 and 41.73. In SLN, although most of cetylpalmitate peaks still remained in the diffractograms, the peaks at 2θ scattered angles of 10.12, 21.65 and 23.84 disappeared (see more details in Appendix D). This shows that cetylpalmitate was in less ordered crystalline form in SLN compared to the bulk cetylpalmitate (Venkateswarlu and Manjunath, 2004). In addition, interaction between SLN ingredient and cetylpalmitate might occur and reduced the intensity of cetylpalmitate peak in SLN. It was observed that there was no foreign peak appearing in diffractgrams of SLN12 and SLN14 containing high content of DDAB and cholesterol, respectively, suggesting that both of DDAB and cholesterol in SLN were in amorphous form. These findings were consistent with the results obtained by DSC technique. That means the SLN prepared by the hot high pressure technique for this study were the true SLN at room temperature.

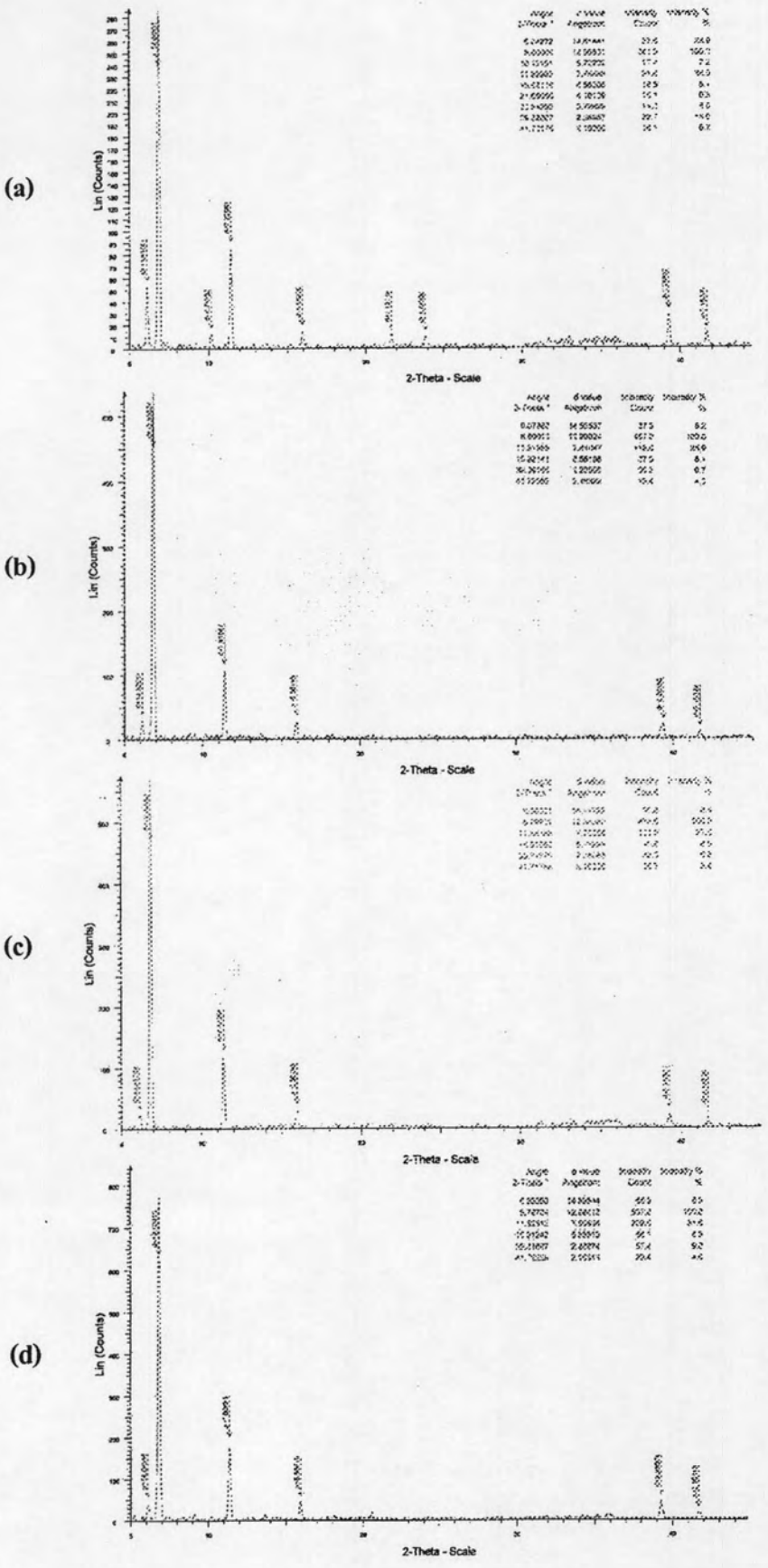

Figure 4.18 XRD patterns of (a) bulk cetylpalmitate, (b) SLN10, (c) SLN12 and (d) SLN14.

1.5 Physical Stability Study of SLN

The SLN9, SLN10, SLN11, SLN12, SLN13, SLN14 and SLN15 stored in air-tight colorless glass bottles at room temperature had been followed changes in their particle size, PI and zeta potential during storage for 60 days. The results are shown in Figure 4.19-4.21. Because Freitas and Müller (1998) showed rapid gelling of the SLN suspension when it was stored in colorless glass under artificial light and data proved that light radiation has a destabilizing effect, therefore, all of SLN studied in this experiment were protected from light by wrapping with aluminium foil.

It was found that most of SLN were quite stable at the storage condition. Their particle diameters, PIs and zeta potentials did not change significantly during 60 days. This might be due to the samples were stored properly apart from the proper ingredients in the formulation. Heurtault et al. (2003) stated that during the development of nanoparticulate structures, the formulation is the first step which might play a role on stability. The composition has to be critically controlled for optimal stability. Finally, external parameters such as temperature and light appear to be of primary importance for long term stability.

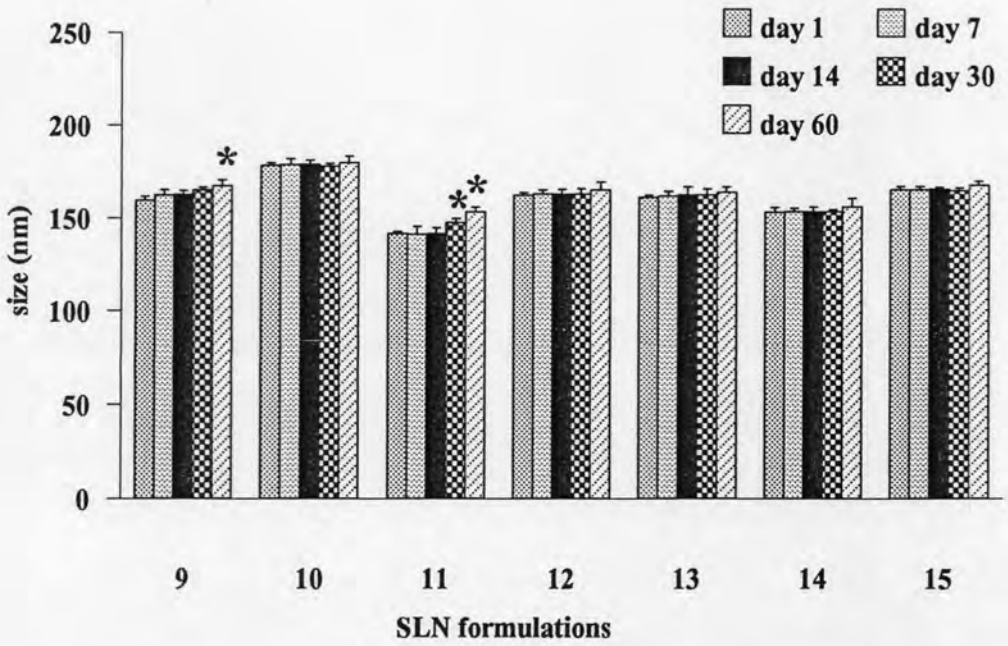

Figure 4.19 Particle size of SLN9-SLN15 measured at day 1, day 7, day 14, day 30 and day 60 (mean±SD, n=3), *significant difference from day 1 (p<0.05).

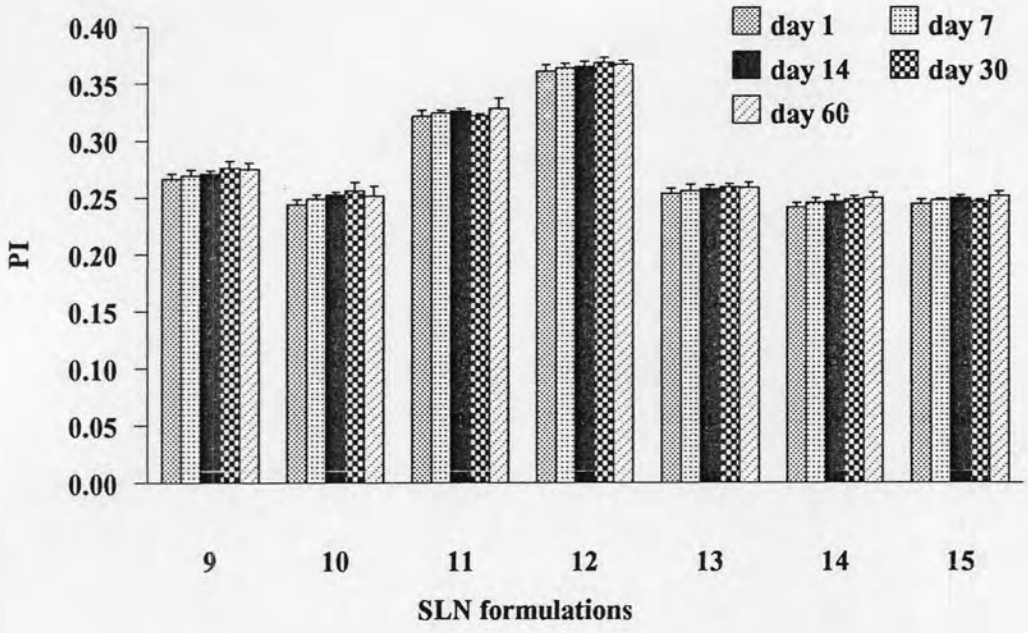

Figure 4.20 PI of SLN9-SLN15 measured at day1, day 7, day 14, day 30 and day 60 (mean±SD, n=3).

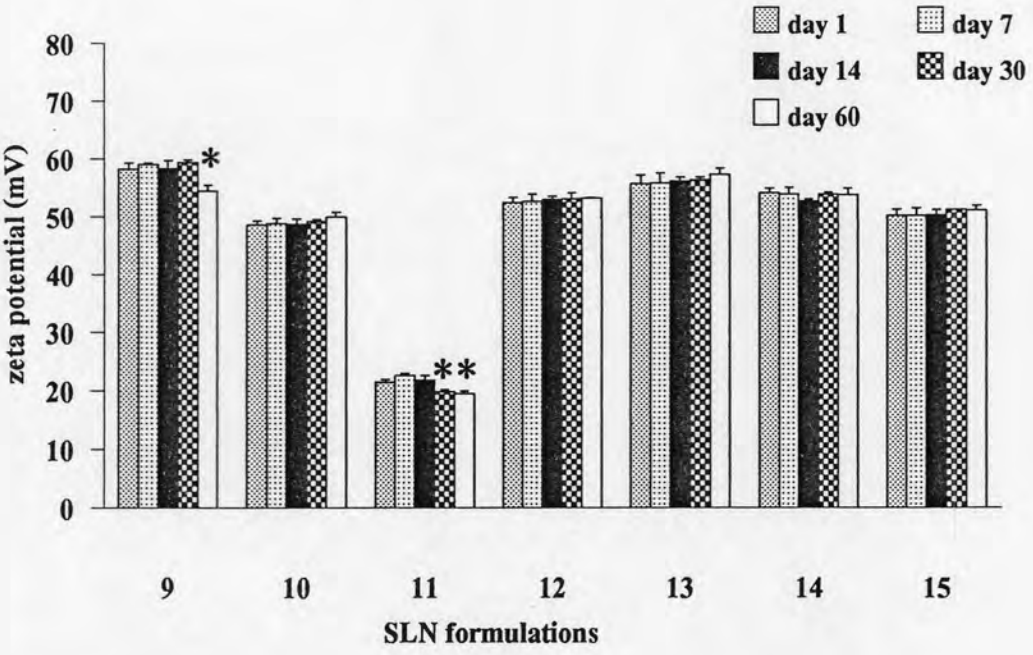

Figure 4.21 Zeta potential of SLN9-SLN15 measured at day 1, day 7, day 14, day 30 and day 60 (mean±SD, n=3), *significant difference from day 1 (p<0.05).

For the effect of temperature, like light exposure, it corresponds to energy input and can lead to changes in the crystalline structure of lipids. Freitas and Müller (1998) proposed that the zeta potential decreases with increasing energy input because it can lead to changes in the crystalline structure of the lipid. Crystalline re-orientation can result in changes of the charges on the particle surface. In addition, different sides of a crystal can possess a different charge density. During one-dimensional growth of a crystal, the surface ratio of differently charged crystal sides changes and consequently, the measured zeta potential changes. They also proposed that when energy input increased, the microviscosity of emulsifier film forming around the particles decreased leading to destabilization of the particles.

Nevertheless, the significant increment of the particle size with the decline of zeta potential was found in SLN9 and SLN11. Figure 4.19 shows that the particle size of SLN9 increased significantly after 2-month storage with p value of 0.031 analyzed by one-way ANOVA while particle size of SLN11 started to increase in the first month of storage with p value of 0.014, and it was larger in the second month with p value of 0.002 compared to the particle size measured at day 1. In the case of SLN9, due to the low content of surfactant, the surfactant films might not be strong enough to prevent agglomeration after particles contacted with others, leading to the particle growth (Jenning, Thünemann and Gohla, 2000) and decline in zeta potential. The instability of SLN11 containing the lowest DDAB content might occur from its lowest zeta potential. Generally, high value of zeta potential of nanoparticles leads to the more physically stable system because the charged particles repel one another by electric repulsion and consequently, overcome the natural tendency to aggregate (Heurtault et al., 2003). Therefore, it has no doubt about the quicker increment in particle size of SLN11 compared to the others. Surprisingly, the PI of SLN9 and SLN11 at the end of storage period were statistically comparable to their PI measured at day 1. This finding could be explained that the change in particle size during storage occurred homogeneously, thus, they were still as homogeneous as they had been at day 1.

2. Preparation and Characterizations of Chitosan Nanoparticles (CSN)

2.1 CSN Production

The CSN produced by ionotropic gelation technique with varying formulation compositions possessed varied particle sizes and positive surface charges shown in Table 4.5. Since chitosan is a weak base polysaccharide containing an average amino group density of 0.837 per disaccharide unit, the amine groups will be then protonated in acidic medium, resulting in a high positive charge. As the charge number of tripolyphosphate, a polyanionic cross-linking agent, also decreases in acidic conditions, the formation of chitosan–tripolyphosphate nanoparticles by ionotropic gelation is highly pH-dependent (Katas and Alpar, 2006). Thus, the pH of CSN prepared in this study was controlled equally to 4.2-4.5 to avoid the pH effect.

Table 4.5 Particle size, PI, zeta potential and pH of CSN (mean±SD)

Formulation	Ratio of chitosan:tripolyphosphate (w/w)	Particle Size (nm)	PI	Zeta Potential (mV)	pH
CSN1	2:1.3	997±2	0.54±0.01	10±0	4.5
CSN2	4:1.3	258±1	0.28±0.00	28±0	4.4
CSN3	8:1.3	866±1	0.43±0.00	39±0	4.2

The appearance of preparations depended on the particle size of obtained CSN. It was observed that the CSN2 looked clearer than those of CSN1 and CSN3 because of its smallest particle size. On the other hand, the CSN1 was more turbid and tended to precipitate more rapidly than other formulations due to its biggest particle size and lowest zeta potential.

Generally, chitosan molecules in aqueous solutions adopt extended conformation with a more flexible chain because of the electrostatic charge repulsion between the chains. When chitosan and tripolyphosphate were mixed with each other, they spontaneously formed compact complexes with size in nanometer range an overall positive surface charge, and the density of the surface charge is reflected by measured zeta potential values (Gan et al., 2005). The tripolyphosphate can interact with chitosan by electrostatic forces linking the ammonium groups of chitosan in the nanoparticle with phosphoric groups of tripolyphosphate molecules. Due to the complexation between oppositely charged species, chitosan undergoes ionic gelation and

precipitates to form spherical nanoparticles (Agnihotri, Mallikarjuna and Aminabhavi, 2004). Figure 4.22 demonstrates morphology of CSN2, a representative, observed by SEM and TEM technique.

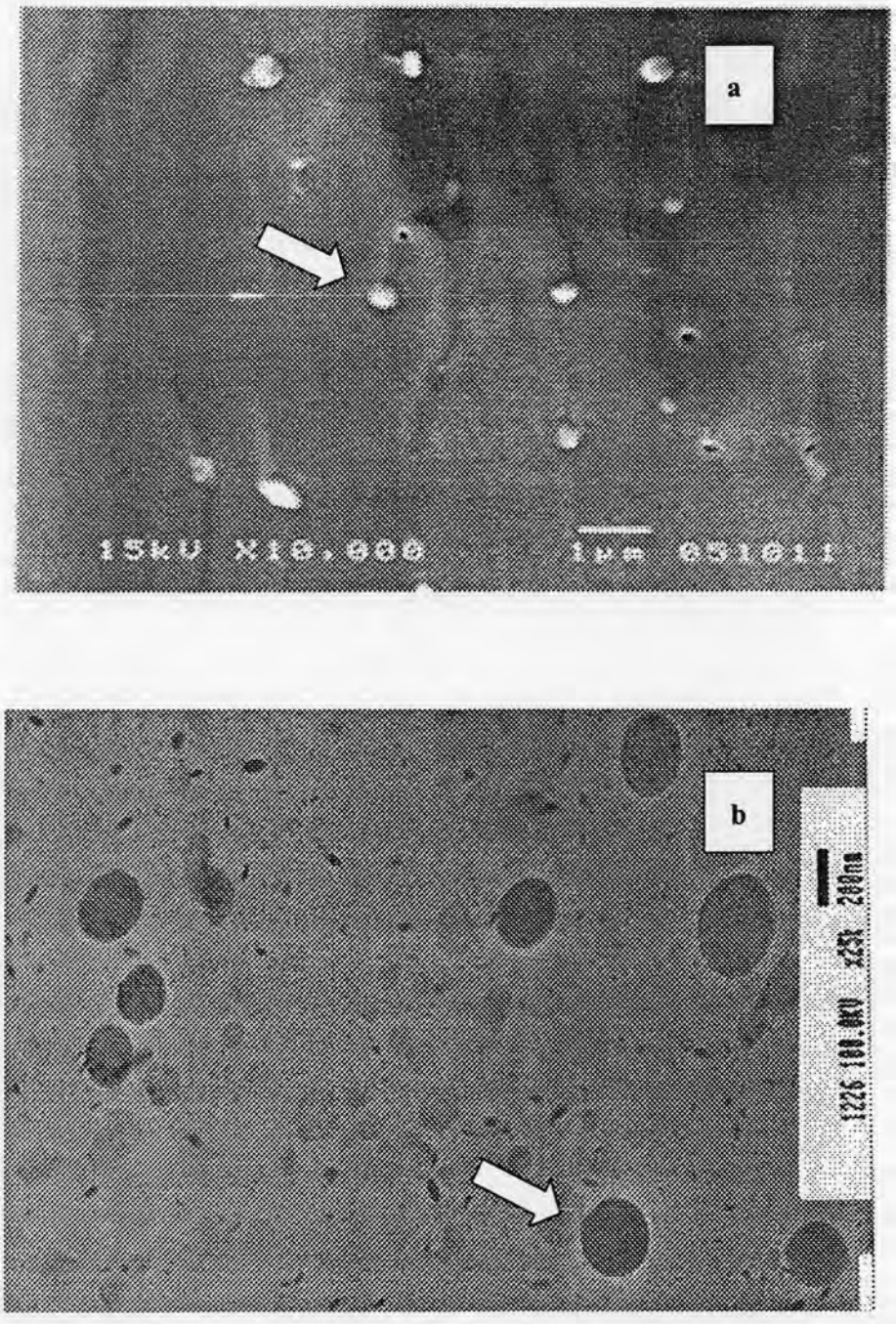

Figure 4.22 Photograph of CSN2: (a) SEM (x10,000) and (b) TEM (x25,000).

The effects of formulation compositions on physicochemical properties of CSN shown in Table 4.5 suggested that the optimum ratio between chitosan and tripolyphosphate led to the CSN possessing small particle size with proper surface charge. It was found that the particle size and zeta potential of CSN increased with the increase in ratios of chitosan to tripolyphosphate from 4:1.3 to 8:1.3. These findings were consistent with the previous work reported by Gan et al. (2005). They found that size, size distribution and also zeta potentail of CSN were mostly affected by the increased chitosan solution concentration, in addition, the increase in size and zeta potential with concentration showed a linear relationship within the tested range. However, the CSN1 prepared by using the lowest chitosan:tripolyphosphate ratio had the biggest size with the lowest zeta potential. This might due to the aggregation of the neutral complex CSN leading to the largest size and also the rapid precipitation. Cui and Mumper (2001) reported the similar finding in their published paper. They found that CSN prepared by ionotropic gelation method with carboxymethylcellulose (CMC) as a polyanion provided the nanometer size of chitosan-CMC complexes for all of the chitosan:CMC ratios investigated (1:1.5, 1:1-8:1 w/w) except for the 1:1.5 which had a relatively larger size (652±205 nm) and lower zeta potential value (8.3±1.6 mV). In fact, the 1:1.5 chitosan/CMC complex was very closed to the neutral point of the complex (1:1.7). This result strongly suggests that the larger size of the 1:1.5 complex was due to aggregation of the neutral complex. Consequently, the CSN2 possessing the proper particle size and surface charge was selected for further study.

2.2 Physical Stability Study of CSN

The CSN2 stored in air-tight colorless glass bottles at room temperature and protected from light by wrapping with aluminium foil had been observed for any changes in its particle size, PI and zeta potential during storage for 60 days. The results are shown in Figure 4.23.

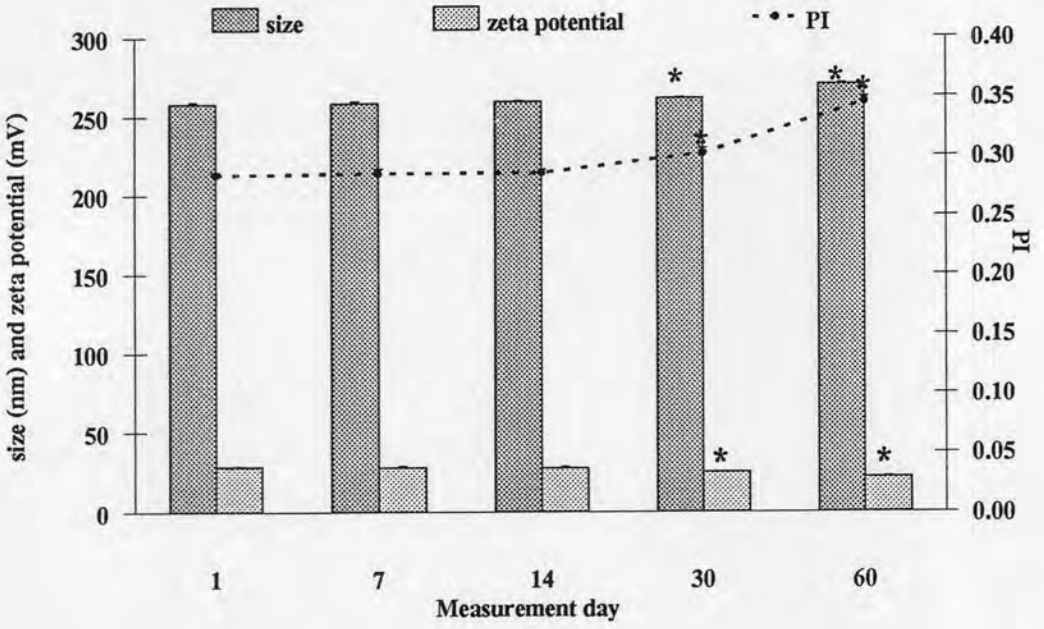

Figure 4.23 Particle size, PI and zeta potential of CSN2 measured at day 1, day 7, day 14, day 30 and day 60 (mean±SD, n=3), *significant difference from day 1 (p<0.05).

Figure 4.23 shows that the particle size of CSN2 started to increase in the first month of storage with p value of 0.014, and it was larger in the second month with p value<0.0001 compared to the particle size measured at day 1 analyzed by one-way ANOVA. Their PI also increased markedly with p value of 0.004 and p<0.0001 for the day 30 and day 60, respectively. In addition, zeta potentials measured at day 30 and day 60 were significantly lower than the zeta potential measured at day 1 with p<0.0001. This suggests that CSN2 was absolutely unstable at the storage condition after 30 days of storage. Therefore, to make sure in its stability, the CSN for the further study must be freshly prepared before using not more than 14 days. The tendency of physical instability found in CSN2 was consistent with the previous work reported by López-León et al. (2005). The authors proposed that the instability of CSN might occur from the erosion of CSN leading to losing their spherical shape in an aqueous environment and their zeta potential. The change of particle morphology increases the diffusion coefficient of the particles and induces particles aggregation. Moreover, polydispersity increments due to the lack of sphericity bear a high uncertainty in the measurement. Thus, the chitosan-tripolyphosphate nanogels behave as a metastable system, therefore, they should be stored in lyophilized form, or freshly prepared when required.

3. Ability of SLN and CSN to Form Complex with pHIS-HIV-hugag

SLN9 to SLN15 and all of CSN used in this study were able to immobilse pDNA in a supplied electric field at the varying nanoparticles:pDNA ratios by forming nanoparticles-pDNA complexes except for SLN11 (Table 4.6). Figure 4.24 shows rafts of nanoparticles after they formed complex with pHIS-HIV-hugag.

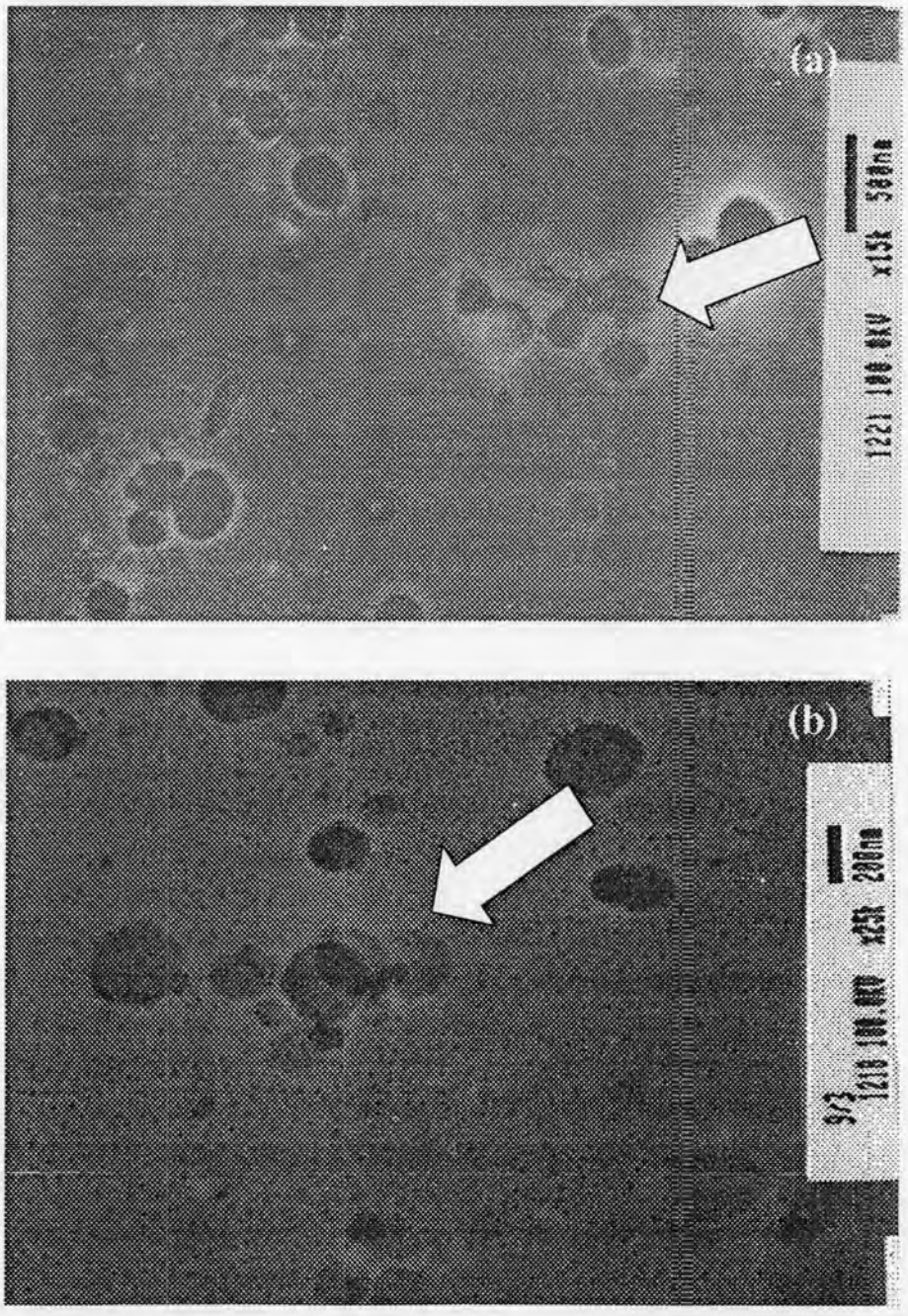

Figure 4.24 TEM photographs of (a) SLN15- (x15,000) and (b) CSN2-pHIS-HIV-hugag complexes (x25,000).

Table 4.6 Nanoparticles: pHIS-HIV-hugag immobilized ratio (w/w)

Formulation	Nanoparticles:pHIS-HIV-hugag immobilized ratio
SLN9	5,000:1
SLN10	10,000:1
SLN11	n/a*
SLN12	5,000:1
SLN13	1,000:1
SLN14	1,000:1
SLN15	1,000:1
CSN1	5,000:1
CSN2	500:1
CSN3	100:1

*not available

For the SLN, the addition of cationic lipid into SLN provided a multivalent positive surface charge that could interact via electrostatic with the negative charge on the pDNA phosphate backbone (Pang et al., 2002). Because the ability of nanoparticle to form complex with pDNA depended mainly on positive surface charge of nanoparticle (Roland and Sullivan, 2003), SLN11 possessing the lowest zeta potential could not bind to pDNA at any ratios. According to statistical analysis of zeta potential by one-way ANOVA with Tukey's multiple comparison at p value of less than 0.05, the SLN containing different surfactant contents; SLN10 and SLN15 possessed a comparable zeta potential but their ability to form complex with pDNA were not equivalent. It was found that SLN15 consisting lower surfactant content began to form complex with pDNA at the SLN:pDNA ratio=1,000:1 while SLN10 was able to immobilize pDNA at 10,000:1. This was probably that the more excess surfactant molecules accumulating on SLN10 surface led to the weak electrostatic interaction between surface of SLN and pDNA. They could not immobilize pDNA in the electric field at the lower ratio of SLN:pDNA. Although the SLN15 contained more surfactant content and possessed less zeta potential than that of SLN9, its ability to form complex with pDNA was greater. This result showed that the optimum surfactant content on SLN surface played an important role on pDNA interaction. Moreover, it might cause any additional interaction between SLN surface and pDNA apart from the electrical interaction such

as hydrophobic force between the surfactant adsorbed on surface of SLN and pDNA (Pang et al., 2002). Due to insufficient positive charges of SLN11 with the lowest DDAB content, it could not form complex with pDNA at any ratios. Surprisingly, although SLN12 possessed a comparable zeta potential to that of SLN15, it retained pDNA in the electric field at higher ratio of SLN:pDNA. This might be the excess DDAB covering the SLN12 surface led to the reduction of interaction between the surface of SLN and pDNA. Therefore, the pDNA was easily detached by the electrical force. SLN13, SLN14 and SLN15 containing varying cholesterol contents formed complex with pDNA at the same ratio of SLN:pDNA=1,000:1. There was no doubt about the ability of SLN13 and SLN14 exhibiting comparable zeta potential. But SLN15 containing medium cholesterol level and possessing a significantly lower zeta potential than that of SLN13 could immobilize pDNA at the same ratio. The result here confirmed that not only the electrical force affected the ability of SLN to form complex with pDNA but also the additional interaction between surface of SLN and pDNA. Therefore, SLN13, SLN14 and SLN15 were selected for further study due to their lowest immobilized ratio of SLN:pDNA.

Although the CSN had lower zeta potential than those of SLN, they can immobilize pHIS-HIV-hugag under electrical field tightly with the lower ratios. This might be due to the strong interaction i.e. electrical interaction and hydrophobic interaction between CSN surface and pDNA. Because the SLN surface was covered by some of cholesterol, surfactant and DDAB molecules, the interaction between particles surface and pDNA at low SLN:pDNA ratio was not sufficient to overcome the electrical force leading to the easy detachment of pDNA from the SLN surface as seen in Figure 4.25. Moreover, Table 4.5 and Table 4.6 suggest that CSN containing more chitosan content started to retain pHIS-HIV-hugag at lower ratios compared to the CSN consisting of less chitosan content. This was due to the CSN containing high chitosan content possessed higher positively charged. Although CSN2 could immobilize pHIS-HIV-hugag at the higher CSN:pHIS-HIV-hugag immobilized ratio than that of CSN3, their particle size was in nanometer range that was more proper for using as pDNA vector than CSN3. Consequently, CSN2 was selected for the further study.

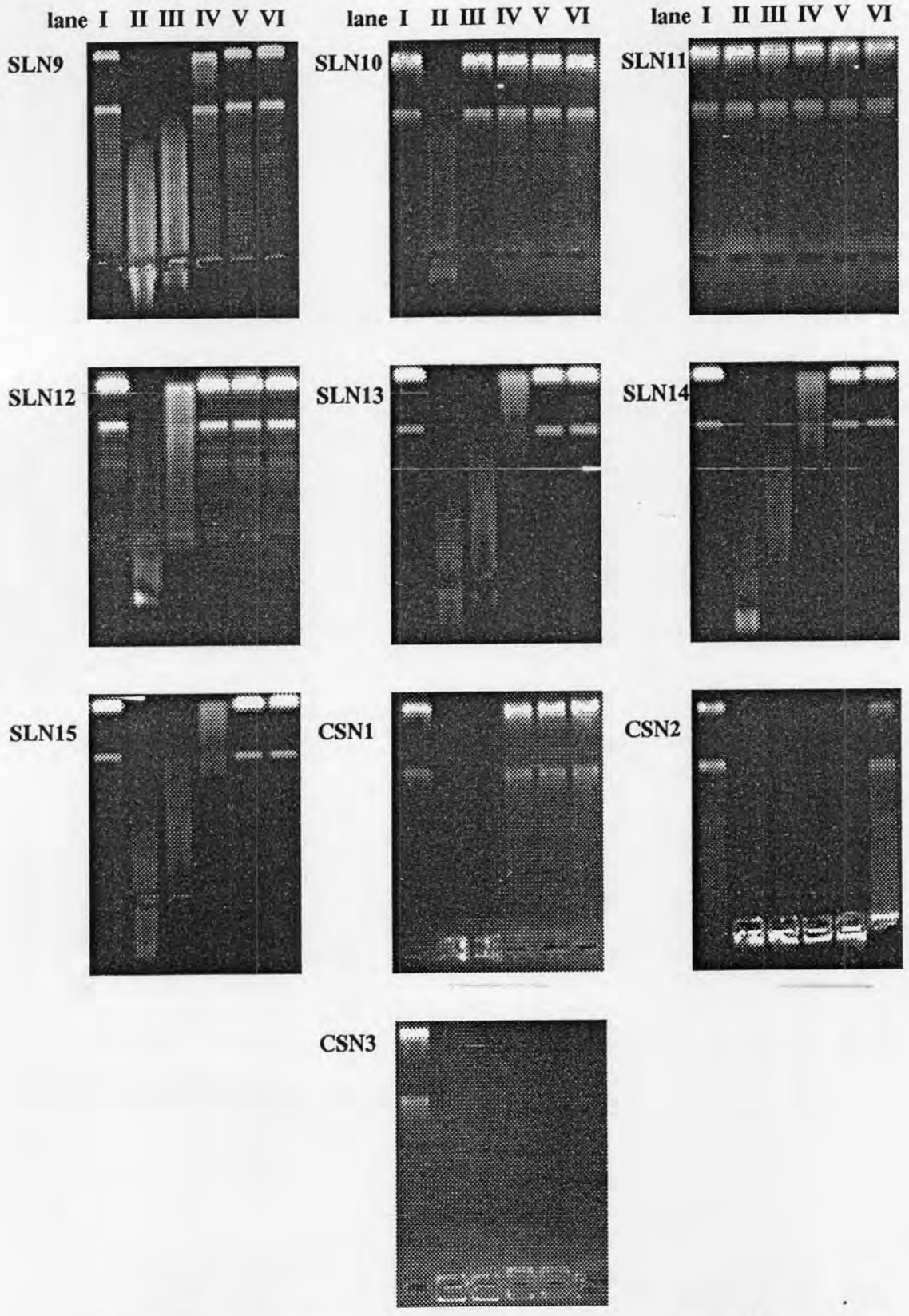

Figure 4.25 Agarose gel electrophoresis of SLN- and CSN-pHIS-HIV-hugag complex; lane I: naked pHIS-HIV-hugag, lane II: nanoparticles:pDNA=10,000:1, lane III: 5,000:1, lane IV: 1,000:1, lane V: 500:1, and lane VI: 100:1.

4. Cytotoxicity Assay

In vitro cytotoxicity assay was performed in HeLa cells by determining the ability of cells to reduce the oxidised blue form of chromogenic indicator to be a reduced pink form.

(a)

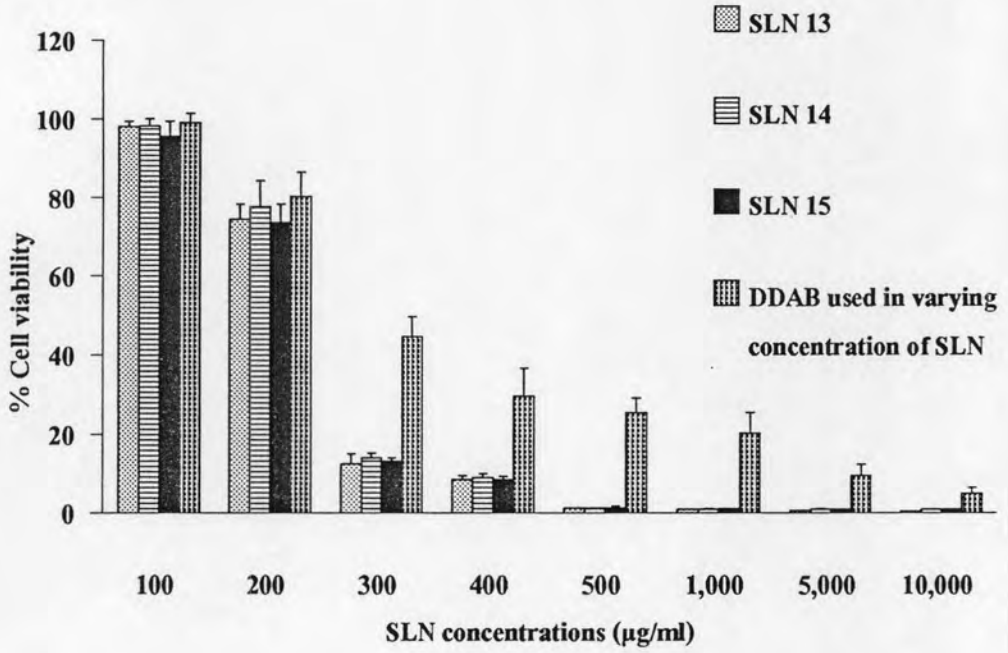

(b)

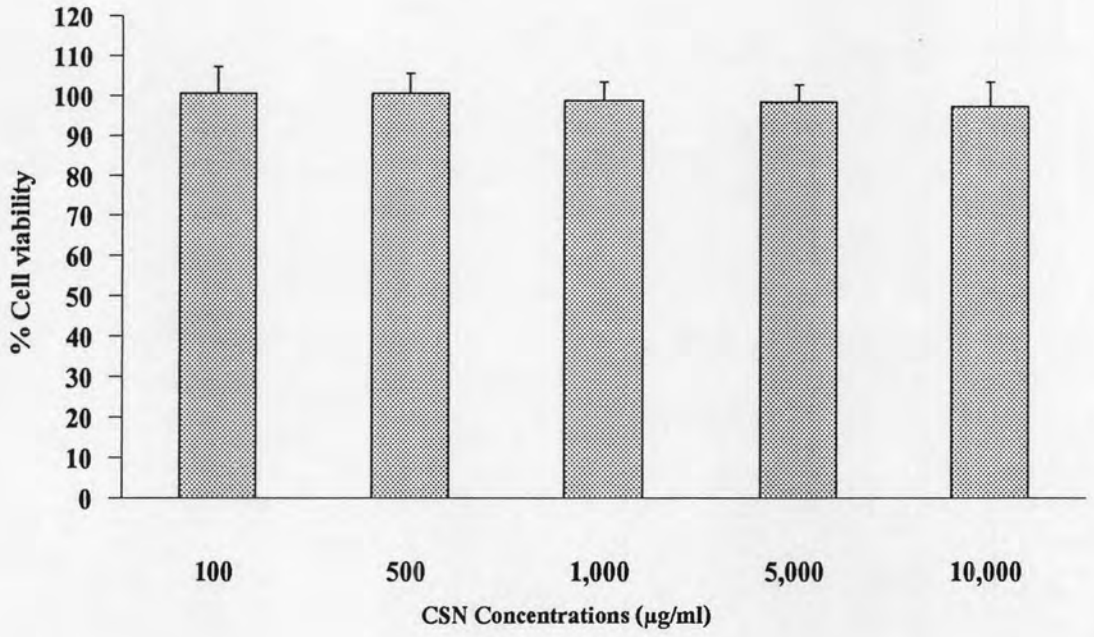

Figure 4.26 %Cell viability of HeLa cells incubated in varying concentrations of (a) SLN and (b) CSN2, (mean± SD, n=4).

The viability of HeLa cells after incubation with varying concentrations of SLN or CSN in DMEM without FBS for 24 hours is shown in Figure 4.26 (a)-(b). The results showed that high concentrations of SLN13, SLN14 and SLN15 were very toxic to cells that only 0.1-15% of HeLa cells still survived in a range of 300 to 10,000 μg/ml of SLN in DMEM. However, most of them were viable in 100-200 μg/ml of SLN in DMEM. Although cetylpalmitate, Tween 80 and Span 85 are accepted as generally recognized as safe substance (Wissing, Kayser, and Müller, 2004), the toxicity of SLN might occur by the toxicity of a cationic lipid, DDAB, synergisted with other formulation compositions as seen in the results of cytotoxicity test of DDAB used in varying concentrations of SLN13, SLN14 and SLN15 in HeLa cells. Tabatt, Sameti et al. (2004) demonstrated that SLN containing DDAB was more toxic to COS-1 cells than SLN containing EQ1 or DOTAP but less toxic than SLN made from CPC or CTAB. This might be that the ester bonds in EQ1 and DOTAP molecule allowed them to be metabolized easily in mammalian cells while DDAB containing two aliphatic chains directly linking to amine group was hardly transformed. By the proper selection of DDAB concentrations, the successful transfection was demonstrated in COS-1 cells using β-galactosidase pDNA.

The Figure 4.26 (b) shows that HeLa cells can servive in 100-10,000 μg/ml of CSN in DMEM with 100% cell viability indicating that CSN2 was absolutely not toxic to HeLa cells. This might due to the formulation compositions of CSN2 were generally accepted as safety chemical. The LD_{50} of chitosan in laboratory mice is 16 g/kg body weight, which is closed to sugar or salt. It is also proven to be safe in rats up to 10% in the diet (Agnihotri et al., 2004). In addition, tripolyphosphate used as polyanion cross-linker which is the most extensively used in production of CSN by ionotropic gelation technique is the one accepted for being used in pharmaceutical application because of its non-toxic property (Gan et al., 2005; López-León et al.,2005).

5. Transfection Study

This experiment was performed to investigate the potential of SLN and CSN for using as *in vitro* pHIS-HIV-hugag transfection vectors. Therefore, the high selectivity technique for specific protein detection used in the previous work (Egan et al., 2006), the western blot technique, was selected to detect the gag protein expressed in HeLa cells.

The transfection study was performed by using SLN and CSN at the concentration of 200 μg/ml that would form complex with 0.4 μg pDNA at the ratio of nanoparticles:pDNA=1,000:1 in 2.0 ml of incubation medium. It was found that a very low intensity of gag protein band could be obtained in cell lysates from HeLa cells incubated with SLN14-pDNA complexes for 4 hours as seen in Figure 4.27 (lane VII) while in lysates from cells incubated with SLN13-, SLN15- or CSN2-pDNA complexes or naked pDNA, the gag protein could not be detected (data not shown).

Figure 4.27 Gag protein in cell lysates from HeLa cells incubated with Fugene 6-, SLN- and CSN-pHIS-HIV-hugag complexes for 24 hours detected by western blot technique; lane I: CSN2-, lane II : Fugene 6-, lane III: SLN14-, lane IV: SLN15-, lane V: SLN 13-, lane VI: naked pHIS-HIV-hugag, lane VII: SLN14-pHIS-HIV-hugag complexes incubated for 4 hours, and lane VIII: marker (24.4 kDa).

The intensity of gag protein band in Figure 4.27 were more intensed when HeLa cells were incubated with nanoparticles-pDNA complexes up to 24 hours. Nevertheless, the gag protein could not be observed from cells incubated with naked pDNA (lane VI). This showed that HeLa cells could be transfected with pHIS-HIV-hugag by using these cationic nanoparticles. Furthermore, it was visually observed that HeLa cells incubated with SLN14-pDNA complexes (lane III) expressed more gag protein than those of cells incubated with SLN15- (lane IV), SLN13- (lane V), naked pDNA, including CSN2-pDNA complexes (lane I). The results here suggested that the SLN containing high cholesterol content could increase gag protein expression in HeLa cells. This might be the activity of cholesterol which is usually used as a helper lipid in cationic liposomes (Cui and Mumper, 2002; Hung et al., 2005; Wiethoff et al., 2001). The more cholesterol, the more rigidity of SLN surface led to protecting themselves from degradation in endosome before reaching cytosol. This property is very important *in vivo* to prevent destabilization of complex before it reaches its target tissue (Roland and Sullivan, 2003). Although the smallest complex size of SLN14-pDNA (322±2 nm) might be taken into cell by endocytosis easier than those of larger nanoparticles-pDNA complex; SLN13-pDNA complex

(375±3 nm), SLN15-pDNA complex (352±1 nm), and CSN2-pDNA complex (366±2 nm) (Pang et al., 2002), the difference of complex size was too small, therefore, the effect of complex size might not affect the endocytosis by HeLa cells in this case. Consequently, SLN14 was selected as a representative of SLN for the further study.

However, when the transfection potential of SLN and CSN was compared to the established transfection agent used in the previous work (Egan et al., 2006), Fugene 6 (lane II), they were ranked only low to moderate level. This suggested that although the obtained SLN and CSN had ability to use as a transfection vector, their composition should be reformulated to improve their potential for *in vitro* transfection.

6. Mice Immunization

The ability of SLN14 and CSN2 for using as pDNA vaccine delivery system was investigated. The nanoparticles-pHIS-HIV-hugag complexes were administered to mice intradermally and transdermally. The IgG specific to the expressed antigen, gag protein (p24 protein), was quantified by ELISA technique.

The gag protein-specific IgG titers from mice immunized intradermally and topically with nanoparticles-pHIS-HIV-hugag complex are shown in Figure 4.28.

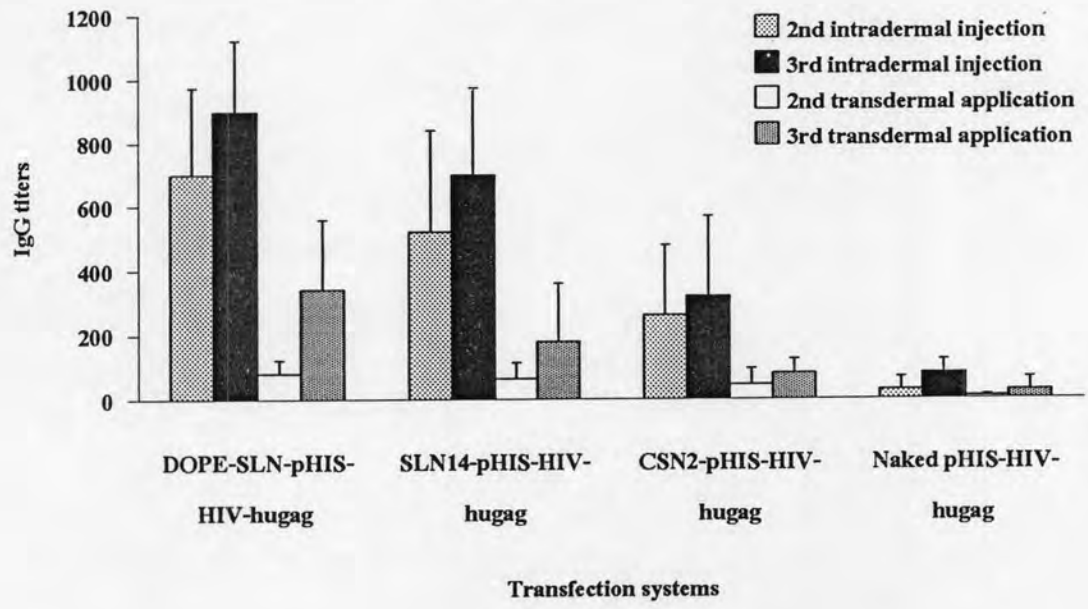

Figure 4.28 Mean IgG titers against gag protein in mice serum determined at day 6 after the second and the third pHIS-HIV-hugag immunization (mean±SD, n=5).

According to statistical analysis by one-way ANOVA with Tukey's multiple comparison at p value of less than 0.05, the IgG titers obtained after the second and the third immunization from mice immunized intradermally were statistically higher than the IgG titers obtained from mice immunized topically. Except for the IgG titers obtained from mice immunized with naked pHIS-HIV-hugag by either intradermal injection or topical application, they were comparable. This might be that the bioavailability of pHIS-HIV-hugag delivered topically was lower than those of bioavailability of pHIS-HIV-hugag delivered by intradermal injection due to the skin barrier that might limit the absorption of pHIS-HIV-hugag. Because of the highly organized structure of stratum corneum, it is regarded as the rate-limiting factor in the penetration of therapeutic agents through the skin especially the compounds with a molecular weight > 500 Da can not cross the stratum corneum easily (Foldvari, 2000).

Due to the intradermal injection is designed to place pDNA in contact with keratinocytes and professional APCs at the edge of dermal level, therefore, pHIS-HIV-hugag injected directly into dermal layer of skin would then bypass the stratum corneum penetration, the rate-limiting step of skin permeation. In addition, the needle injection may puncture cell, thereby, directly transfecting a few cells resulting in the higher probability of pDNA taken up into cells compared to some applied on skin. Furthermore, some of the pHIS-HIV-hugag injected went into the superficial dermis allowed some expression occurred in the epidermis cells, especially the epidermis keratinocytes and accessing to Langerhan cells (Peachman, Rao and Alving, 2003).

The IgG titers obtained from mice immunized with naked pHIS-HIV-hugag by either intradermal injection or topical application were comparable. This might be that the naked pHIS-HIV-hugag delivered intradermally was subjected to rapid degradation by biological environments (Panyam and Labhasetwar, 2003) leading to the low amount of pHIS-HIV-hugag at target site besides the low transfection efficiency of naked pDNA itself.

The Figure 4.28 also shows that the IgG titers obtained after the third immunization were higher than the IgG titers obtained after the second immunization. This might due to the immune response to early antigenic exposure requires processing and presentation of the antigen to helper T-lymphocytes including the processing of the protein antigen expression, moreover, the presence of memory lymphocytes at the late exposure to the same antigen bypasses the lengthy antigen processing and presentation processes (Shen and Louie, 1999).

The results shown in Figure 4.28 suggested that the IgG titers obtained after the third immunization from mice immunized intradermally with DOPE-SLN was the highest. This might be that DOPE, a neutral helper lipid, could increase the transfection efficiency of pHIS-HIV-hugag in dermal layer by its endosomolytic activity (Babiuk et al., 2000; Cui and Mumper, 2002; Tabatt, Kneuer et al., 2004; and Watabe et al., 2001).

The membrane destabilizing activity of DOPE causes the rupture or lysis of the endosome membrane and allows the release of pDNA into the cytosol. This fact has been attributed to the ability of DOPE by its tendency to undergo a transition to a hexagonal configuration under acidic pH, which may facilitate fusion with or destabilization of target membranes, in particular endosomal membranes (Pedroso de Lima et al., 2001). The pHIS-HIV-hugag could then enter the nucleus via action of its nuclear localization signal to activate gene expression (Farhood et al., 1995; and Huang et al., 1995). Although the cholesterol has also been accepted as a helper lipid, its efficacy for transfection helping is lower than that of DOPE leading to the lower transfection efficiency compared to DOPE-SLN and lower elicited immune response (Cui and Mumper, 2002).

The IgG titers obtained from mice immunized intradermally with CSN-pHIS-HIV-hugag was quite low. This might due to the low transfection efficiency of CSN in dermal layer. However, there was no doubt about the lowest IgG titers obtained from mice immunized with naked pHIS-HIV-hugag because of its low transfection efficiency and easy degradation in biological environment.

Moreover, the Figure 4.28 shows that topical immunization with the both of SLN-pHIS-HIV-hugag elicited significantly greater IgG titers against gag protein than the naked gene ($p< 0.05$); in contrast, topical immunization with CSN-pHIS-HIV-hugag was comparable to that provoked by the gene alone. These could be explained by the low transfection efficiency of CSN in skin layer.

7. Skin Penetration Pathway of Nanoparticles-pHIS-HIV-hugag Complex Study

The Figure 4.29 shows that red fluorescence from the nanoparticles-rhodamine-labeled pHIS-HIV-hugag complex could be detected on the porcine skin surface after they were applied for 24 hours. That means some of rhodamine-labeled pHIS-HIV-hugag still located on the stratum corneum without penetration within 24 hours. This might be that the penetration through skin of pHIS-HIV-hugag was limited by stratum corneum.

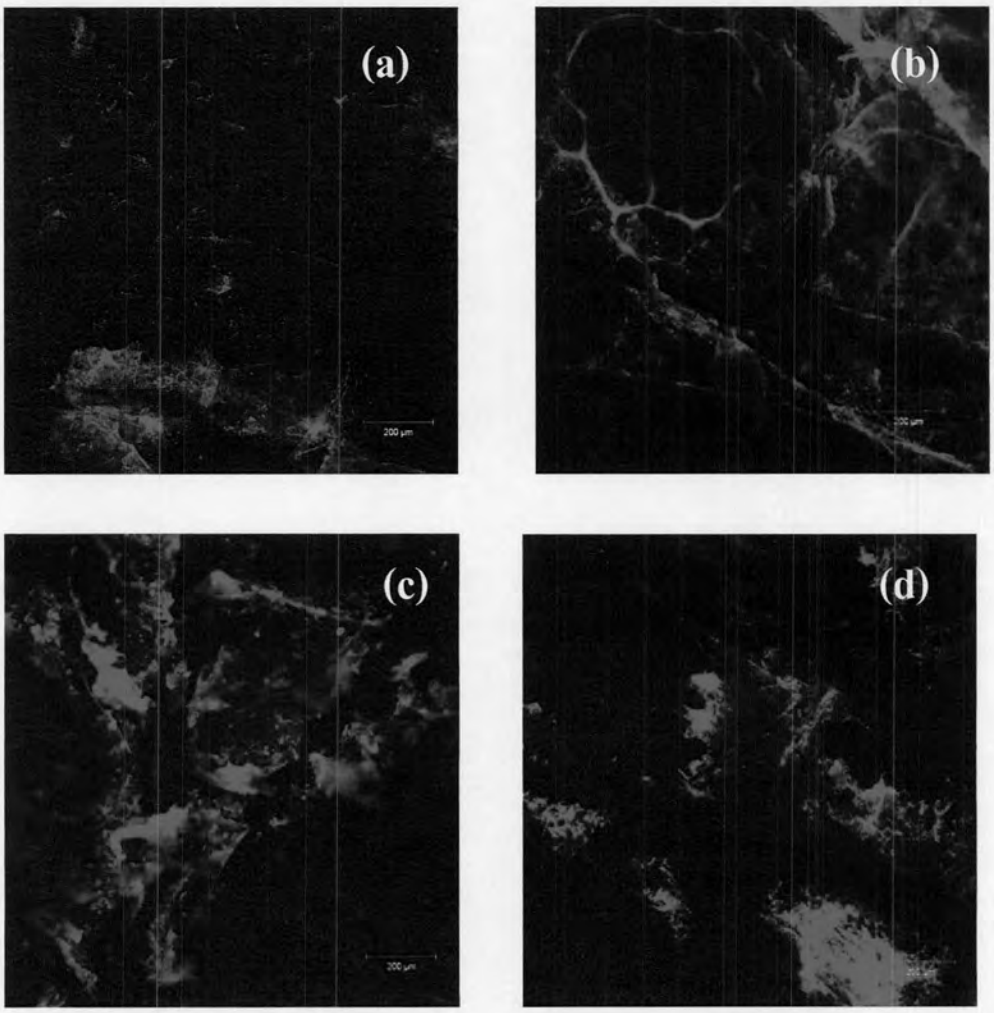

Figure 4.29 Confocal micrographs of the skin surface subsequent to treatment with nanoparticles-rhodamine-labeled-pHIS-HIV-hugag for 24 hours; (a) DOPE-SLN-pHIS-HIV- hugag, (b) Chol-SLN-pHIS-HIV-hugag, (c) CSN-pHIS-HIV-hugag, and (d) naked-pHIS-HIV-hugag.

A useful way to consider factors affecting drug permeation rate through stratum corneum is via the simple equation for steady state flux, equation (4.4). The cumulative mass of diffusant, m, passing per unit area through the membrane, at long times is defined as steady state flux (dm/dt) (Barry, 1983)

$$\frac{dm}{dt} = \frac{DC_0K}{h} \qquad (4.4)$$

where C_0 is a constant concentration of drug in donor solution, K is the partition coefficient of solute between membrane and bathing solution, D is the diffusion coefficient and h is thickness of membrane.

From the equation (4.4), the ideal properties of a molecule penetrating stratum corneum should possess low molecular mass, preferably less than 500 Da, when *D* tends to be high. Its solubility in oil and water should be optimum to provide the optimum partition coefficient (Barry, 2001). Therefore, the pHIS-HIV-hugag possessing a size of 5,079 bp (about 1,810 Da) with high water solubility could penetrate through stratum corneum difficultly, especially when it formed complex with nanoparticles, the larger size obtained. This assumption was proved by the high intensity of rhodamine-labeled pHIS-HIV-hugag observed on skin at varying depth from surface of stratum corneum seen in Figure 4.30 obtained by orthogonal section mode.

The picture (a) and (b) show that the signal of rhodamine is very intense on the stratum corneum as seen in high intensity of the upper position signal when the orthogonal line was drawn across the cluster of corneocytes. However, the lower position of the signal was also observed when the orthogonal line was drawn across junctions of the cluster of corneocytes. This suggested that the nanoparticles-pHIS-HIV-hugag complexes still located on skin surface although they had been applied on the skin for 24 hours. Nevertheless, some of them can penetrate deeply into skin via the junctions of cluster of corneocytes. Considering the picture (c) and (d), most of signal is found in the upper position confirming that most of the complexes deposited on the upper skin.

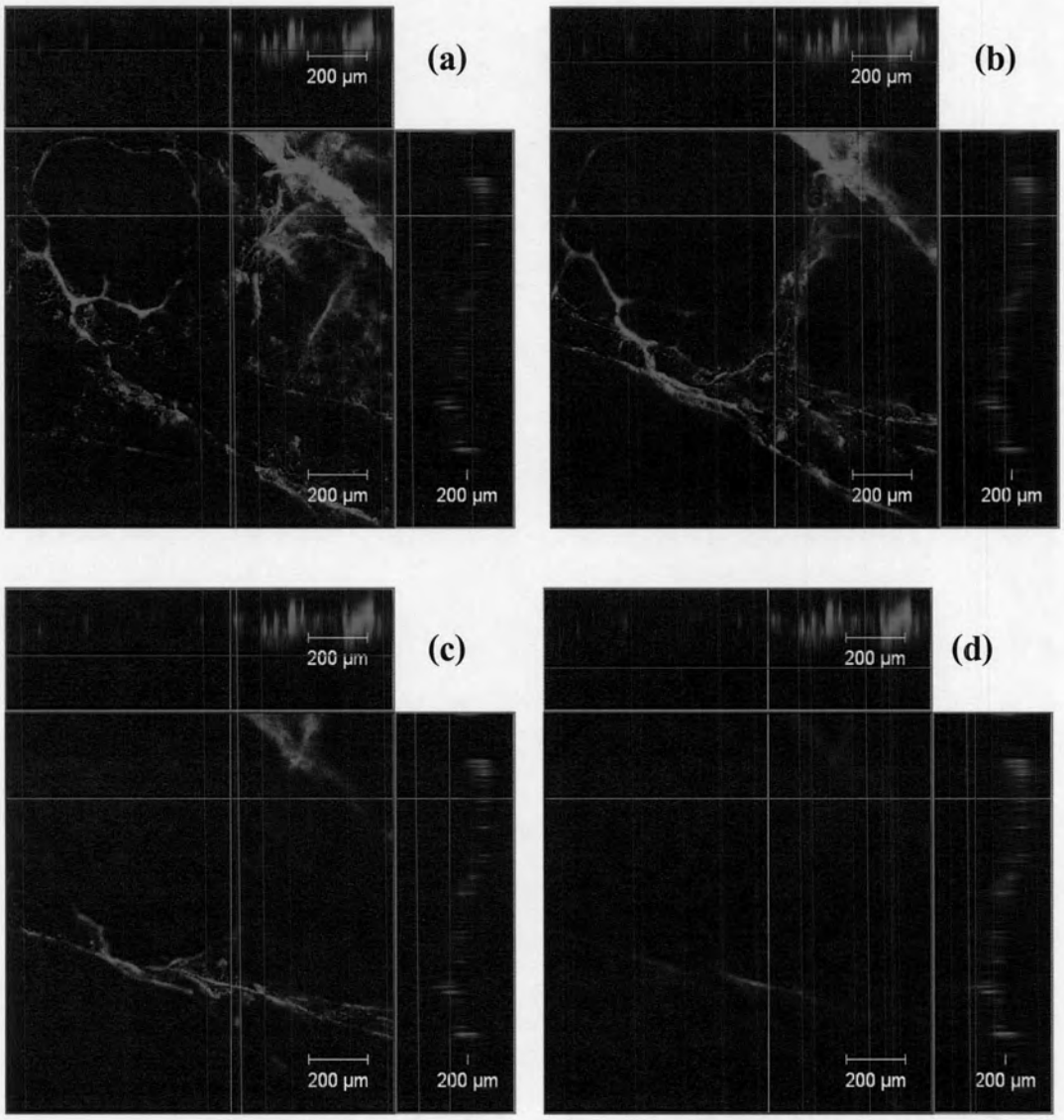

Figure 4.30 Orthogonal section of porcine skin after 24-hour passive diffusion of Chol-SLN-rhodamine labeled-pHIS-HIV-hugag complex varied the depth from surface of stratum corneum; (a) 39.3 µm, (b) 78.6 µm, (c) 118.0 µm, and (d) 157.3 µm.

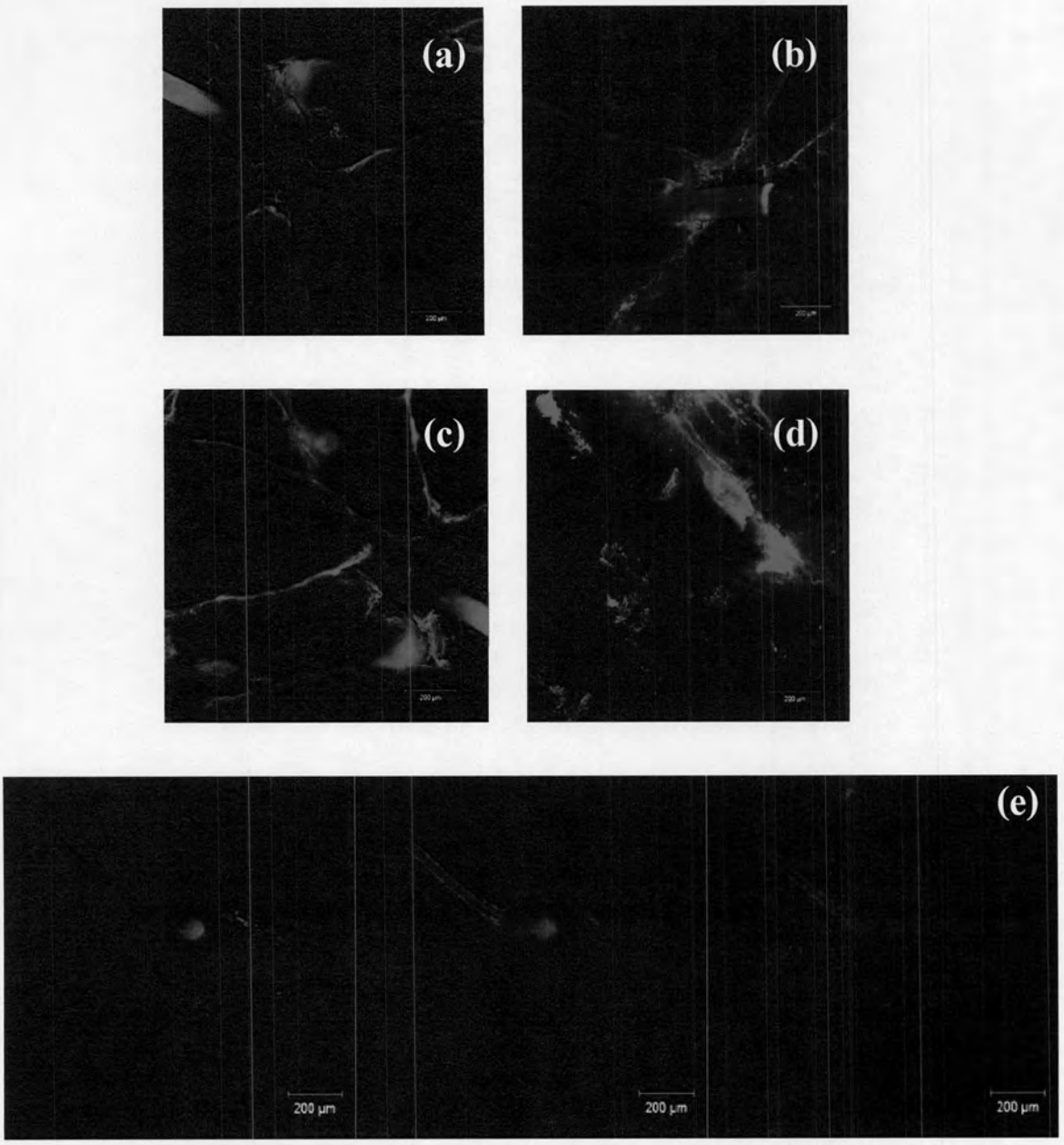

Figure 4.31 Confocal micrographs of hair follicles and pilosebaceous units subsequent to treatment with nanoparticles-rhodamine-labeled-pHIS-HIV-hugag for 24 hours; (a) DOPE-SLN-pHIS-HIV-hugag, (b) Chol-SLN-pHIS-HIV-hugag, (c) CSN-pHIS-HIV-hugag, (d) naked-pHIS-HIV-hugag, and (e) CSN-pHIS-HIV-hugag distributing in pilosebaceous unit.

Figure 4.31 shows that some of fluorescent nanoparticles-pHIS-HIV-hugag distributed in hair follicles (Figure 4.31 (a)-(d)) and sebaceous gland (Figure 4.31 (e)). This finding was consistent with the distribution of liposome-pDNA complexes reported by Birchall et al. (2000) and Weiner (1998). This also indicated that pilosebaceous delivery is a physicochemical property specific to nanoparticles-pDNA complexes (Niemiec et al., 1997).

Barry (2001) proposed that pilosebaceous unit provides a route that bypasses intact stratum corneum. This might be due to the sebaceous gland cells are more permeable than corneocytes and thus drug can reach the dermis by entering the follicle passing through the sebaceous gland or penetrating the epithelium of follicular sheath. The rich blood supply aids absorption, even though the shunt route cross-sectional area is small. Therefore, the pDNA immunized topically could elicit the specific immune response. In addition, at the junction of stratum corneum with the hair follicle there is a lipophilic matrix of triglycerides, waxy esters and cholesterol, which collectively form sebum. This pocket of oily substance forming the entrance to the pilosebaceous unit is approximately 70 μm in diameter. It can be envisaged that the physicochemical properties of lipid-pDNA complexes allow for partition into sebum with access directly to cell of the pilosebaceous unit (Birchall et al., 2000).

Besides their large complex size, tightly binding between CSN and pHIS-HIV-hugag might cause pDNA could not dissociate from complexes to move to nucleus leading to low transfection efficiency and consequently, comparable IgG titers to that elicited by topical naked pDNA immunization. In addition due to the hydrophilic property of CSN, interaction between complexes might occur more than the interaction of CSN complexes-oil substance when they were dispersed in oil-rich pilosebaceous unit leading to CSN complexes aggregation. Therefore, endocytosis by follicular cells including sebaceous gland cells occurred difficultly causing lower IgG titers in mice immunized topically with CSN-pHIS-HIV-hugag compared to SLN-pHIS-HIV-hugag. This finding was consistent to the previous work performed by Cui and Mumper (2001). They found that topical CSN-β-galactosidase pDNA complexes immunization could elicit IgG titer to express β-galactosidase protein at the same level of naked pDNA. Surprisingly, chitosan oligomer/CMC nanoparticles could elicit more IgG titers.

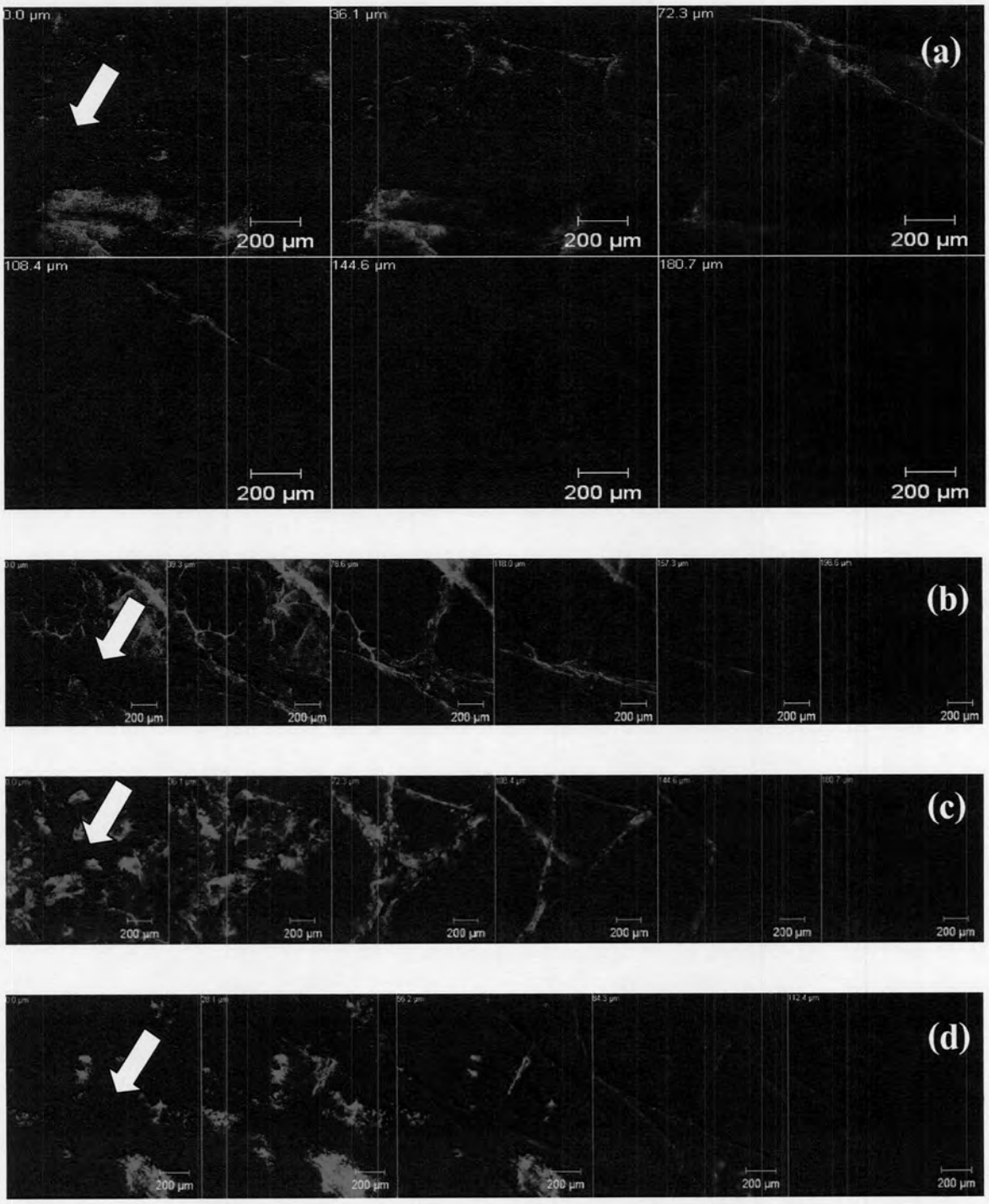

Figure 4.32 The z-series of confocal images obtained following 24 hours of passive diffusion of nanoparticles-rhodamine labeled-pHIS-HIV-hugag from surface of stratum corneum (0 µm); (a) DOPE-SLN-pHIS-HIV-hugag, (b) Chol-SLN-pHIS-HIV-hugag, (c) CSN-pHIS- HIV-hugag, and (d) naked-pHIS-HIV-hugag.

The z-series of images from stratum corneum surface into skin shown in Figure 4.32 indicates that the fluorescent nanoparticles-pHIS-HIV-hugag complexes were observed in skin furrows at depths up approximately 150-200 μm. The labeled, naked gene, on the other hand, was not localized so far into the barrier (~100 μm). This implies that the nanoparticles may provide improved substantivity such as skin retention and protection from biodegradation, thereby allowing a longer residence time on the tissue (Panyam and Labhasetwar, 2003). In addition, the results of confocal microscopy experiment suggest that the major skin penetration pathway of either nanoparticles-pHIS-HIV-hugag complexes or naked pHIS-HIV-hugag are pilosebaceous units and skin furrows.

It was observed that the tendency of the skin permeation result performed by z-stack technique was consistent with the magnitude of gag-specific IgG titers obtained from mice immunized topically with nanoparticles-pHIS-HIV-hugag except for the CSN-pHIS-HIV-hugag case. This implies that the nanoparticles could facilitate the pHIS-HIV-hugag to penetrate deeply into skin and also increase transfection efficiency of the pDNA in skin layer. Although the CSN-pHIS-HIV-hugag complex could penetrate more deeply than those of naked pHIS-HIV-hugag, the elicited IgG titers obtained from mice immunized topically with either CSN-pHIS-HIV-hugag or naked pHIS-HIV-hugag were statistically comparable. This confirms that the transfection efficiency of pHIS-HIV-hugag delivered by CSN in skin cells was as low as the naked pDNA.